The Astrophysical Journal, 1005:34 (20pp), 2026 July 1 https://doi.org/10.3847/1538-4357/ae75b0
© 2026. The Author(s). Published by the American Astronomical Society.
OPEN ACCESS

MXDFz4.4: A LyC Emitter 250 Myr after the Epoch of Reionization and a First Test of Lyα Morphology as a Tracer of LyC Escape at High Redshift

Ilias Goovaerts[1], Marc Rafelski[1,2], Alexander Beckett[3], Grecco Oyarzún[2,4], Annalisa Citro[5], Farhanul Hasan[1], Kalina V. Nedkova[6], Calum Hawcroft[1], Anton M. Koekemoer[1], Mitchell Revalski[1], Matthew J. Hayes[7], Claudia Scarlata[5], Ray A. Lucas[1], Norman A. Grogin[1], David V. Stark[1,2], Paolo Suin[8], Nor Pirzkal[1], and Louis-Gregory Strolger[1]

[1] Space Telescope Science Institute, 3700 San Martin Drive, Baltimore, MD 21218, USA; igoovaerts@stsci.edu
[2] Department of Physics and Astronomy, Johns Hopkins University, Baltimore, MD 21218, USA
[3] Aix Marseille Université, CNRS, CNES, LAM (Laboratoire d'Astrophysique de Marseille), 13388 Marseille, France
[4] Homer L. Dodge Department of Physics and Astronomy, The University of Oklahoma, 440 W. Brooks St., Norman, OK 73019, USA
[5] Minnesota Institute for Astrophysics, School of Physics and Astronomy, University of Minnesota, 316 Church Street SE, Minneapolis, MN 55455, USA
[6] IPAC, Mail Code 314-6, California Institute of Technology, 1200 E. California Blvd, Pasadena, CA 91125, USA
[7] Department of Astronomy and Oskar Klein Centre for Cosmoparticle Physics, Stockholm University, AlbaNova University Centre, SE-10691, Stockholm, Sweden
[8] Université Paris-Saclay, Université Paris Cité, CEA, CNRS, AIM, 91191, Gif-sur-Yvette, France
Received 2026 March 3; revised 2026 May 29; accepted 2026 May 30; published 2026 June 23

Abstract

Assessing the contribution of ionizing sources to cosmic reionization is a central goal of extragalactic astrophysics. Understanding and quantifying ionizing escape remains challenging near the Epoch of Reionization. We present the highest-redshift Lyman continuum (LyC) emitter detected to date, MXDFz4.4, at $z = 4.442$ in the MUSE eXtremely Deep Field, observed only ∼0.25 Gyr after the end of reionization. A high-confidence Lyα line confirms the redshift. LyC flux is detected at 5.3σ in the F435W filter with a flux of 4.2 ± 0.8 nJy, corresponding to a flux measurement at 5.2σ. After correcting for the intrinsic production of LyC photons and the intergalactic medium opacity at $z = 4.44$, we derive high escape fractions, $f_{\rm esc}$, ranging from 50% to 100%. We apply established low-redshift tracers of LyC escape and, for the first time at this redshift, promising Lyα morphological tracers such as the halo fraction (HF). Spectral energy distribution fitting indicates the presence of a recent burst of star formation; we explore its impact on the production and escape of ionizing photons. Lyα-based tracers of $f_{\rm esc}$ reveal a complex scenario in which the recent burst strongly influences LyC production and escape, combined with a more evolved stellar population. This interpretation is supported by UV diagnostics, including $\Sigma_{\rm SFR}$ and sSFR. Our results provide cautious support for the Lyα HF as a LyC escape tracer at high redshift. Considering the burst-driven enhancement in ionizing photon production and escape, we conclude that stochastic star formation in the early Universe likely plays a significant role in the contribution of galaxies to cosmic reionization.

Unified Astronomy Thesaurus concepts: Galaxies (573); Reionization (1383); Lyman-alpha galaxies (978); Starburst galaxies (1570)

1. Introduction

The contribution of ionizing sources to the process of cosmic reionization is a central topic of extragalactic astrophysics and a key goal of the JWST mission. With the first years of JWST data, significant progress has been made in two of three necessary quantities to constrain this contribution: the star formation rate (SFR) density and the production of ionizing photons (per unit SFR). The SFR density during the Epoch of Reionization (EoR) is determined by the UV luminosity function, which has been robustly constrained with photometry (C. T. Donnan et al. 2024; S. L. Finkelstein et al. 2024; Y. Asada et al. 2026) and spectroscopy (Y. Harikane et al. 2024) up to $z \sim 13$. Similarly, the production of ionizing photons has been quantified by recent works (C. Simmonds et al. 2023; M. J. Hayes et al. 2025; M. Llerena et al. 2025; A. Pahl et al. 2025), with excellent statistics, revealing only slight or no evolution with redshift. The third necessary quantity, the escape fraction of ionizing photons, $f_{\rm esc}$, remains elusive.

Ionizing flux cannot be directly observed in the EoR, due to absorption of ionizing photons by the intervening neutral H I gas in the intergalactic medium (IGM). Therefore, $f_{\rm esc}$ must first be understood at lower redshifts and indirect tracers established, which we can use to quantify the escape of ionizing photons within the EoR. Significant progress has been made in recent years by the Low-z Lyman Continuum Survey (LzLCS; S. R. Flury et al. 2022a; see also J. Chisholm et al. 2022; A. Le Reste et al. 2025)—which has studied in detail 35 Lyman continuum emitters (LCEs) at $z \sim 0.3$—and by other studies (Y. I. Izotov et al. 2016, 2020, 2022, 2024b; A. Verhamme et al. 2017; see A. E. Jaskot 2025 for a review). The most important findings are that (i) Lyα properties, such as equivalent width (EW) and escape fraction ($f_{\rm esc,Ly\alpha}$), correlate well with $f_{\rm esc}$ (A. Henry et al. 2015; A. Verhamme et al. 2017; C. C. Steidel et al. 2018; S. R. Flury et al. 2022b) and that (ii) the Lyα line separation from the systemic redshift and the halo fraction (HF) show a strong anticorrelation with $f_{\rm esc}$ (A. Verhamme et al. 2015; Y. I. Izotov et al. 2018b, 2020; S. R. Flury et al. 2022b; A. Saldana-Lopez et al. 2026).

Original content from this work may be used under the terms of the Creative Commons Attribution 4.0 licence. Any further distribution of this work must maintain attribution to the author(s) and the title of the work, journal citation and DOI.

Combined, these results connecting Lyα and Lyman continuum (LyC) emission highlight the importance of clear channels in H I column density in allowing the escape of Lyman photons from the interstellar medium (ISM) of the host galaxy.

Other galaxy properties that have been found to correlate well with f_{esc} include SFR surface density, Σ_{SFR} (Y. I. Izotov et al. 2016; E. Vanzella et al. 2018; S. R. Flury et al. 2022b; A. E. Jaskot et al. 2024), steep, blue UV slopes (β; J. Chisholm et al. 2022; Z. Ji et al. 2025), the strength of the [O III]/[O II] ratio (Y. I. Izotov et al. 2018b, 2020; A. E. Jaskot et al. 2024), and the presence of strong UV lines such as C IV λ1550 (A. Saxena et al. 2022; D. Schaerer et al. 2022; Y. I. Izotov et al. 2024a). High Σ_{SFR} likely contributes to the creation of clear channels crucial to LyC escape, steep UV slopes are attributed to the role of dust in blocking LyC photons, and high [O III]/[O II] ratios in LCEs have been associated with sensitivity to the ionization parameter and feedback from massive stars.

However, no single tracer alone reliably predicts the escape of ionizing photons, underscoring the need for a framework that both links the escape of LyC photons to available tracers and assesses the importance of different variables in tracking the escape of LyC photons, such as in M. Maji et al. (2022) and A. E. Jaskot et al. (2024). We have reached the point that such multivariate predictors can be used on the appreciable sample of low-redshift LCEs collated in the literature and on simulated data (J. Rosdahl et al. 2022; N. Choustikov et al. 2024). However, due to a lack of data as comprehensive as the LzLCS for a statistically significant population at $z > 2$, we are not yet at this stage at these redshifts.

At $z > 2$, which we term "high redshift" for the purposes of this work, a number of open questions remain. Recent studies have cast doubt on the ability of Lyα properties to reliably trace f_{esc} at high z (M. J. Rutkowski et al. 2017; J. Kerutt et al. 2024; A. Citro et al. 2025). For instance, A. Citro et al. (2025) found galaxies with strong Lyα emission but without traces of LyC emission at the expected strength based on low-z estimators. J. Kerutt et al. (2024) found a diversion from the well-established relation at low redshift between f_{esc} and Lyα peak separation (Y. I. Izotov et al. 2018b), as well as large scatter in the well-established Lyα EW and f_{esc} relation (C. C. Steidel et al. 2018).

Therefore, doubts persist over the applicability of low-redshift f_{esc} tracers during the EoR, which is their primary purpose. As $\sim$10 Gyr of evolution have taken place between the EoR and low-redshift measurements, there are numerous factors that may influence the universal validity of f_{esc} tracers. Examples include the merger fraction, known to increase with redshift (V. Rodriguez-Gomez et al. 2015), the evolution of the star formation efficiency (P. Madau et al. 1996), and the UV background (X. Fan et al. 2006). It is therefore important to search for LCEs as close to the EoR as possible.

In this work, we describe the detection of an LCE at $z = 4.442$, within $\sim$0.25 Gyr of the EoR, in the MUSE eXtremely Deep Field (MXDF; R. Bacon et al. 2023), which we henceforth refer to as MXDFz4.4. In Section 2, we describe the MUSE data used to detect the Lyα line, which confirms the redshift, as well as the Hubble Space Telescope (HST) and JWST data used to detect the LyC flux and characterize the spectral energy distribution (SED) of the galaxy. Section 3 describes MXDFz4.4 and the necessary modeling to derive its properties: SED fitting and modeling of IGM transmission. We evaluate all accessible f_{esc} tracers that have been established at low redshift, focusing on the important Lyα–LyC connection, in Section 5. Finally, we interpret this discovery in relation to the transmission of the IGM and the properties of MXDFz4.4 in Section 6, offering conclusions in Section 7.

Throughout this paper, we adopt a value for the Hubble constant of $H_0 = 70\,\mathrm{km\,s^{-1}\,Mpc^{-1}}$, and the cosmology used is $\Omega_\Lambda = 0.7$ and $\Omega_m = 0.3$. All initial mass functions (IMFs) used are stated throughout the text and magnitudes are given in the AB mag system (J. B. Oke & J. E. Gunn 1983). All EWs are given in the rest frame unless otherwise stated.

2. Data and Analysis

The MXDF (GTO Program 1101.A-0127; PI: R. Bacon, R. Bacon et al. 2023) is a region of extremely deep observations by the MUSE integral field spectrograph on the Very Large Telescope, with the deepest area having a total exposure time of 141 hr. MUSE has a field of view of $1 \times 1'$, with a spatial pixel size of $0\farcs2$. The spectra have a wavelength range of 4700–9350 Å and a spectral pixel size of 1.25 Å. This wavelength coverage enables MUSE to detect Lyα emission in the redshift range $2.9 < z < 6.7$. All MXDF data are publicly available[9] and viewable using a web interface.[10]

The MXDF is situated within the footprint of the Hubble Ultra Deep Field (HUDF; S. V. W. Beckwith et al. 2006), with additional public HST Advanced Camera for Surveys (ACS)/Wide Field Camera (WFC) and Wide Field Camera 3 (WFC3)/UVIS imaging from programs including GOODS (M. Giavalisco et al. 2004), CANDELS (N. A. Grogin et al. 2011; A. M. Koekemoer et al. 2011), 3D-HST (G. B. Brammer et al. 2012), UVCANDELS (X. Wang et al. 2025), UVUDF (H. I. Teplitz et al. 2013), and HDUV (P. A. Oesch et al. 2018). The HST filters used in this analysis are WFC3/UVIS F336W and ACS/WFC F435W, F606W, F775W, F814W, and F850LP. The F435W filter, in which MXDFz4.4's LyC emission is detected, has an average depth of 150 ks. These data have been reprocessed as part of HST archival program PID 16621 (PI: Koekemoer), including calibration improvements from updated darks, biases, flat-fields and astrometric alignments, as well as other low-level improvements including improved removal of cosmic rays, satellite trails, and bad pixels.

This field also benefits from public JWST imaging from the JADES and JEMS programs (M. J. Rieke et al. 2023; C. C. Williams et al. 2023; D. J. Eisenstein et al. 2026),[11] where the JWST/NIRCam filters from these programs that we use are F090W, F115W, F150W, F182M, F200W, F210M, F277W, F335M, F356W, F410M, F430M, and F444W. F460M and F480M are also included in the JADES imaging data release (M. J. Rieke et al. 2023); however, we exclude these filters from our SED fitting, as visual inspection revealed elevated background levels relative to the source signal in these bands, rendering the photometry unreliable and the associated uncertainties likely underestimated.

2.1. Photometry of MXDFz4.4

We perform custom photometry on the full-resolution images to maximize the resulting flux signal-to-noise ratio

[9] https://amused.univ-lyon1.fr
[10] https://amused.univ-lyon1.fr/project/UDF/browse
[11] DOIs: M. Rieke et al. (2023) and C. Williams et al. (2023).

(SNR) of MXDFz4.4. The segmentation map released by the JADES collaboration blends MXDFz4.4 with a faint neighbor to the southeast, so we create a custom version where these sources are carefully deblended. We perform Kron photometry (R. G. Kron 1980) on the full-resolution images and correct these values by 10%, consistent with curve-of-growth analysis checks we performed. We note that the neighbor is very faint, so this has minimal effects on the photometry published in M. J. Rieke et al. (2023).

As the emission in F435W is spatially far more compact than in redder filters, we apply a different method to maximize the SNR in the F435W image, similarly to the method used by M. Rafelski et al. (2015) and L. Sun et al. (2024) for faint UV photometry of the UVUDF and UVCANDELS surveys. Specifically, we calculate an isophotal flux using a segmentation map based on the F606W filter, a neighboring filter where MXDFz4.4 is more compact than the detection image used by JADES but with high enough SNR to create a reliable segmentation map. This smaller aperture fully captures the flux in the F435W filter and reduces the contribution from sky-dominated pixels, thereby increasing the SNR of the flux measurements. The uncertainty on the flux within the aperture is calculated using the F435W rms map and propagated with the uncertainty on the sky background subtraction, which is done in a wide annulus around MXDFz4.4, ensuring no flux from any object is taken into account.

We connect the F435W flux to the rest of the photometry by using an aperture correction based on the larger JADES-based isophotal area. This correction is determined by taking the ratio of the isophotal flux measured in the smaller and larger isophotal areas in the F606W image. This correction assumes that the distribution of flux is similar in F606W and F435W, which is confirmed both visually and by comparison with the F435W flux measured in the larger isophotal area. The two flux measurements agree within the smaller isophotal area uncertainties, as expected. This F606W isophotal area flux measurement is then used to define the SNR of the detection. The F435W detection significance is 5.3σ.

To verify that correlated noise or large-scale noise patterns do not affect this detection, we calculate the flux in 1,000,000 empty sky apertures of the same size as the aperture used to detect MXDFz4.4's F435W flux. Apertures are placed at random positions across the image, avoiding regions containing detected sources. A histogram of these fluxes is shown in Figure 1, with MXDFz4.4's detection flux shown with a green solid line coincident with the 5σ threshold shown in the dotted–dashed gray line. The width of this distribution agrees with the formal uncertainty from the rms map, indicating that correlated noise and large-scale patterns do not significantly affect the LyC flux measurement in F435W.

We correct for the effects of the point-spread function (PSF) by applying published encircled energy corrections (similar to PSF matching) to the resultant Kron photometry, which is reasonable given the compactness of our galaxy.[12,13] The alternative standard method of PSF matching the images before measuring the photometry would reduce the SNR of the F435W photometry, as it would smooth the flux over the larger

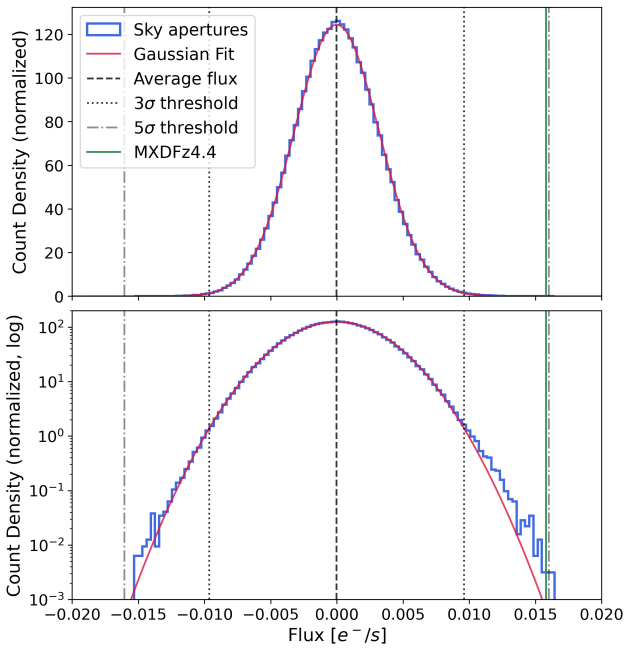

Figure 1. The flux in 1,000,000 empty sky apertures is shown as a histogram along with a Gaussian fit to those fluxes. The detection flux of MXDFz4.4 is shown as the green solid line, coincident with the 5σ threshold shown in the dotted–dashed gray line. The agreement between this empirical test and the formal uncertainty from the rms map demonstrates the robustness of our LyC detection in F435W. The lower plot has a logarithmic y-axis to better visualize the high-flux tail of the distribution.

F444W PSF and thus increase our flux uncertainty. We confirm the validity of this method in two ways. First, we check the curves of growth of the photometry including the encircled energy correction and find convergence at large radii. Second, we compare the photometry of the redder HST and JWST photometry with this method to that of the PSF-matched photometry from JADES, and find good agreement. Therefore, this Kron flux corrected to the total flux (10%) plus the encircled energy correction is used as our final flux measurement. We propagate the uncertainties from each correction accordingly, together with the uncertainty in aperture flux and background subtraction. The resultant LyC flux measurement in F435W is 4.2 $\pm$ 0.8 nJy, at 5.2σ. We subsequently use this photometry for the SED fitting described in Section 3.1.

2.2. Spectral Extraction of MXDFz4.4 from the MXDF Data Cube

The MUSE consortium makes their spectra public, the extraction of which follows R. Bacon et al. (2023). We briefly outline this procedure here, specifically that which relates to extraction using the ORIGIN software (D. Mary et al. 2020), as this is the method used for MXDFz4.4. The ORIGIN software is optimized to detect faint line emitters in MUSE data cubes. Care is taken to mask any bright continuum sources in a three-stage process. The first two stages involve segmenting and masking out any bright, noisy sources, first on the datacube itself, creating a white-light continuum image, then on the SNR residual image thereof. Principal component analysis is then used iteratively to clean further residuals from each spaxel in the cube. Emission lines are then detected by filtering the datacube with possible spectral line profiles. Each source is then extracted from the original datacube using the

[12] HST: https://www.stsci.edu/hst/instrumentation/acs/data-analysis/aperture-corrections.
[13] JWST: https://jwst-docs.stsci.edu/jwst-near-infrared-camera/nircam-performance/nircam-point-spread-functions#NIRCamPointSpreadFunctions-Encircledenergiesforresampleddata.

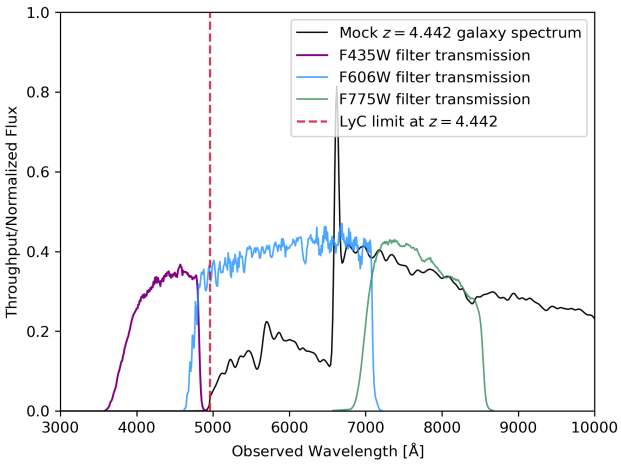

Figure 2. A mock SED of an LAE taken from the JAGUAR mock catalog (C. C. Williams et al. 2018). The LAE has the same redshift as MXDFz4.4 and the F435W filter transmission is plotted in purple, along with a dashed red line delineating the Lyman limit at $z = 4.442$. The F435W filter probes only LyC emission at this redshift. The F606W and F775W filters are also shown; these filters are used for the bands that probe the Lyα and rest-frame UV emission, respectively.

algorithm from K. Horne (1986). These extracted spectra are publicly available for all line emitters detected in the MXDF. We take the spectrum for MXDFz4.4 and apply a custom fitting process, which is described in Section 5.1.1. This process also follows the line-fitting procedure for Lyα lines described in R. Bacon et al. (2023) but allows us to extract and visualize all necessary Lyα properties.

3. Physical Properties of MXDFz4.4

MXDFz4.4 is located in the deepest section of the MXDF (exposure time $\sim$140 hr) at an R.A. and decl. of 53.1577218, -27.7822649, and a redshift (from the Lyα emission line) of 4.442. This makes it the highest-redshift directly observed LCE to date.

MXDFz4.4 has an observed ratio of ionizing to nonionizing flux, $\frac{F_{\rm LyC}}{F_{1500}}$ (in F_ν units) of 0.18 $\pm$ 0.04, calculated from the F435W-to-F775W flux ratio. We adopt the nomenclature $F_{\rm LyC}$ to denote the LyC flux detected in F435W, rather than F_{900}, to differentiate from studies in which the flux at exactly 900 Å is used from spectra. The F435W band covers up to 900 Å rest frame, but as it starts below 700 Å we term this wavelength range "LyC." A diagram of a $z = 4.442$ Lyα emitter (LAE) SED taken from the JAGUAR suite of mock SEDs (C. C. Williams et al. 2018), the F435W filter transmission, and Lyman limit at 912 Å is shown in Figure 2.

The $f_{\rm esc}$ values that we derive, depending on the intrinsic ratio of ionizing to nonionizing flux and the IGM attenuation, are presented in Table 1 and discussed in Section 4. The properties of MXDFz4.4 derived from SED fitting are detailed in Section 3.1, while a detailed analysis of the Lyα emission line observed with MUSE is presented in Section 5.1. The HST and JWST imaging of MXDFz4.4 is shown in Figure 3, and the MUSE spectrum is shown in Figure 4.

While the spectrum shows only a single emission line, MXDFz4.4 has a confident redshift as the line has an asymmetric profile, typical of Lyα emission lines. We include a detailed discussion of how we rule out other possible redshifts in Appendix A. In the same appendix, we calculate the probability of a chance alignment with a low-redshift interloper (0.0076%) and present evidence of the resolved nature of the flux in F435W, ruling out the possibility that the LyC flux originates from a supernova in a faint, low-redshift host galaxy.

No lines other than Lyα are detected in the MUSE spectrum. A redder spectrum of MXDFz4.4 obtained with JWST/NIRISS wide-field slitless spectroscopy as part of the NGDEEP program also exists (PID 2079; PIs: S. Finkelstein, C. Papovich, N. Pirzkal; M. B. Bagley et al. 2024). No lines are detected in the NIRISS spectrum, which is to be expected (see Appendix B for the full details).

3.1. SED Fitting

We use the CIGALE SED-fitting code to derive MXDFz4.4's properties, fitting the observed photometry with a flexible, nonparametric star formation history (SFH). In order to predict the ratio of UV to ionizing photons ($L_{1500}/L_{\rm LyC}$), which we require to calculate the intrinsic escape fraction of MXDFz4.4, we do not include the IGM-affected bands (F606W and F435W; see Section 4). As mentioned in Section 2, we also do not fit the F460M and F480M bands. We fit using two different stellar population synthesis models to assess the impact that this choice has on the derived properties.

The CIGALE SED-fitting code (D. Burgarella et al. 2005; M. Boquien et al. 2019), as used in this work, builds composite stellar populations based on flexible SFHs by combining stellar population synthesis models. In our runs, we use two different sets of models: G. Bruzual & S. Charlot (2003, hereafter BC03) and BPASS v2.2 (J. J. Eldridge et al. 2008, 2017). The BPASS models include the effects of binary populations on stellar evolution. Switching these binary effects on or off, as well as switching between the different extinction laws (Milky Way, LMC, SMC), affects the best-fit galaxy properties. Importantly, the affected properties include the intrinsic $L_{1500}/L_{\rm LyC}$, without a significant change in the reduced chi-squared of the fit. We therefore run CIGALE using the BPASS models in each of these cases (making six separate runs) and utilize the full range of results to report more realistic measurements and uncertainties.

CIGALE also accounts for gas ionized by massive stars, as well as extinction and reemission due to dust, using a modified D. Calzetti et al. (2000) attenuation law. We adopt a Chabrier IMF (G. Chabrier 2003) and a nonparametric SFH with 10 bins covering the past 600 Myr. The most recent bin spans the latest 5 Myr, while the remaining bins are equally sized in log space. The best fit is found with an SFH that remains at a very low level until $\approx$10 Myr before the galaxy is observed, rising into a strong burst in the most recent 5 Myr. The resulting model can be used to predict the intrinsic emission in the LyC regime. By convolving the resulting best-fit spectra with the F435W and F775W filter transmissions, we derive luminosity ratios, $L_{1500}/L_{\rm LyC}$, of 1.01 $\pm$ 0.24 and 1.0–1.2 for the BC03 and BPASS models, respectively. We note that using a 'delayed-τ' SFH model returns very similar results, i.e., the best fit exhibits a strong burst $\approx$5 Myr in the past. The best fits using the BC03 and BPASS models (with the nonparametric SFH) are shown in Figure 5. All results derived from the SED fitting, including the escape fractions (see also Section 4), are given in Table 1. Quantities derived using the BPASS models are given as ranges encompassing the values derived from all six runs.

Table 1
Escape Fraction of MXDFz4.4 and Properties Derived from SED Fitting

$f_{\rm LyC}/f_{1500}$	$L_{1500}/L_{\rm LyC}$	$T_{\rm IGM}$	$f_{\rm esc}^{\rm rel}$ [%]	A_v	$f_{\rm esc,abs}^{\rm IGM}$ [%]
0.18 ± 0.04	3[a]	0.18	300%	0.34[b]–0.68[c]	160–220
	1.0–1.5[d]	0.18	100–150%	0.34[b]-0.68[c]	53–109
	1.01 ± 0.24[b]	0.18			100 ± 32
	1.0-1.2[c]	0.18			100–120
$M_{\rm UV}$	${\rm SFR}_{10}$ [$M_\odot$ yr^{-1}]	${\rm SFR}_{100}$ [$M_\odot$ yr^{-1}]	$M_\star$ [$M_\odot$]		
−18.2 ± 0.1	11.8 ± 0.6[b]	2.4 ± 0.1[b]	$10^{8.3\pm0.2}$[b]		
	1.4–3.3[c]	0.29–1.2[c]	$10^{7.5-8.0}$[c]		

Notes. Properties of MXDFz4.4 related to the escape fraction and host-galaxy parameters derived from SED fitting with CIGALE (see text). The upper table pertains to the escape fraction properties, with the first two rows using luminosity ratios derived from stellar population models, a value commonly assumed in the literature (3; C. C. Steidel et al. 2001; J. Kerutt et al. 2024) and values derived from young, metal-poor pySTARBURST99 models. Both of these rows use the range of dust attenuation values derived by our SED fitting with CIGALE. The final escape fractions are given as a range based on the ranges of $f_{\rm esc}^{\rm rel}$ and A_v. The bottom two rows use the luminosity ratios directly from CIGALE, which already have dust attenuation included. The luminosity ratio from BPASS is given as a range based on different runs (see Section 3.1). All these results use a $T_{\rm IGM}$ value of 0.18 (see text). The lower table contains properties derived from SED fitting of the host galaxy, with the first row using the BC03 models and the second row BPASS. BPASS-derived values are given as ranges based on the values derived from all BPASS runs (see text).
[a] Value from the literature.
[b] Value from fitting with BC03 models (G. Bruzual & S. Charlot 2003).
[c] Value from fitting with BPASS models (J. J. Eldridge et al. 2017).
[d] Value from pySTARBURST99 models (C. Hawcroft et al. 2025).

Due to the likely impact of the recent burst of star formation on $f_{\rm esc}$ (due to stellar feedback clearing holes in the ISM; D. Rahner et al. 2017; M. Trebitsch et al. 2017; C. A. Carr et al. 2025), we additionally consider $L_{1500}/L_{\rm LyC}$ values taken directly from two different stellar population synthesis models of young stars ($\lesssim$10 Myr): BPASS (J. J. Eldridge et al. 2008) and the recent pySTARBURST99 models (C. Hawcroft et al. 2025). Both codes incorporate effects that can be significant for the production of LyC photons. pySTARBURST99 includes the effects of stellar rotation as well as very massive stars (VMSs) up to 300 $M_\odot$ (see Figure 6). BPASS takes into account the effect of binary stellar populations.

CIGALE may struggle to fit a very young population due to a sparsity of very young star templates, additionally motivating an analysis using these specialized stellar models. Both population synthesis codes utilize a similar framework to make predictions of synthetic observables based on grids of input stellar evolution models and spectral libraries. While these codes adopt different stellar libraries, the only significant difference affecting the $L_{1500}/L_{\rm LyC}$ ratio is the inclusion of synthetic VMS spectra: pySTARBURST99 includes synthetic VMS spectra directly, whereas BPASS extrapolates from a regular OB grid (relevant in the first ∼3 Myr). In Figure 6, we show the evolution of $L_{1500}/L_{\rm LyC}$ over the first 10 Myr for a range of metallicities after including the effects of VMSs. The $L_{1500}/L_{\rm LyC}$ ratio derived from CIGALE is consistent with the lower end of the range shown, which supports the idea of a very recent burst in MXDFz4.4. We show the escape fractions derived using the luminosity ratios from these models alongside the CIGALE-derived escape fractions in Table 1. We discuss the consequences for MXDFz4.4's escape fraction in Sections 4 and 6.

3.2. IGM Modeling

The IGM is expected to absorb large fractions of ionizing photons at $z \gtrsim 3.5$ (A. K. Inoue 2011; A. K. Inoue et al. 2014). Despite this, LCEs have been confirmed at redshifts up to $z \sim 4$ (E. Vanzella et al. 2018; U. Meštrić et al. 2025), and candidates exist out to $z \sim 4.4$ (L. J. Prichard et al. 2022; J. Kerutt et al. 2024). The detection of MXDFz4.4 makes it imperative to assess whether an IGM sight line with sufficiently high transmission can account for the observed ionizing flux, or whether this result calls into question our models of IGM transmission near the EoR.

We model the IGM using the TAOIST routine described in R. Bassett et al. (2021). In brief, mock sight lines are populated with H I absorbers at random locations following the redshift-dependent column density distribution function (CDDF) given by C. C. Steidel et al. (2018). We model individual H I absorbers with column densities between 10^{12} and 10^{21} cm^{-2}, producing Voigt profiles with varying Doppler widths at wavelengths redder than 912 Å (sampled from L. Hui et al. 1999). At bluer wavelengths, the absorption cross section is proportional to λ^3 (D. E. Osterbrock 1974). By integrating the transmission curve through our LyC band, we calculate the transmission of the IGM ($T_{\rm IGM}$), i.e., the fraction of flux in F435W that is transmitted through the IGM along a given mock sight line.

To adequately sample the $T_{\rm IGM}$ distribution, we produce 10,000 mock sight lines. The TAOIST code allows for a different CDDF to be adopted for the circumgalactic medium (CGM) of the galaxy, where the higher gas density leads to more high-column-density absorbers. As the redshift of MXDFz4.4 is based on the Lyα line, it is not clear whether there is Lyα emission at the systemic redshift. We therefore produce two sets of mock sight lines: one including absorption from the CGM of MXDFz4.4 and the other assuming a clear channel through the CGM along which LyC photons can escape. The resulting $T_{\rm IGM}$ distributions from both sets of sight lines is shown in Figure 7. Given that MXDFz4.4 must be in a sight line with higher than average transmission, we select the 3σ value from our list of modeled sight lines for use in deriving our escape fractions. This corresponds to $T_{\rm IGM} = 0.18$.

The CDDF used in this modeling was produced using measured H I absorbers at $2.0 \lesssim z \lesssim 2.8$ (G. C. Rudie et al. 2013),

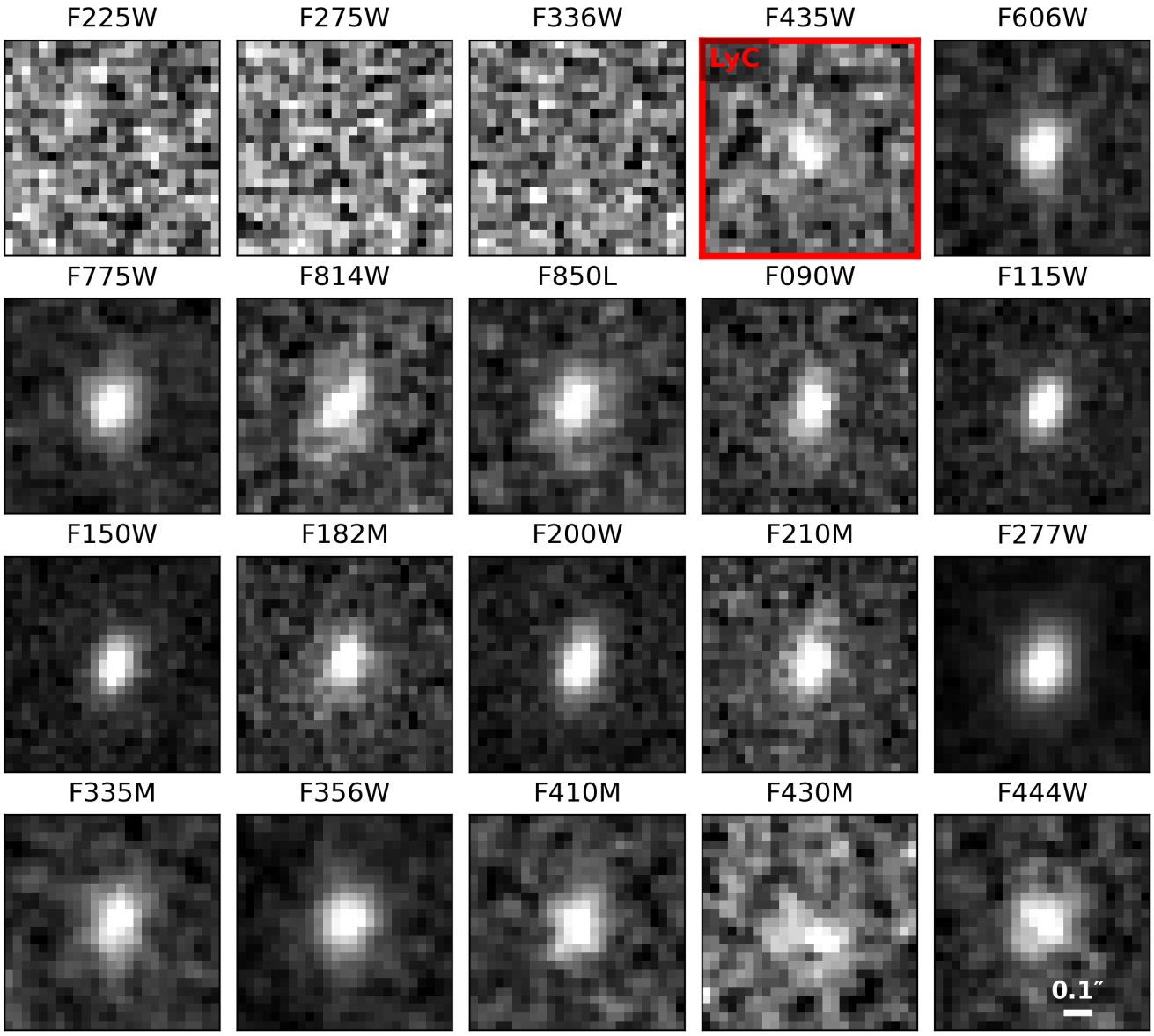

Figure 3. Cutouts of MXDFz4.4 in all filters used for SED fitting, as well as the F225W, F275W, and F336W filters to show nondetections. The HST data reduction is outlined in Section 2, and the remaining (JWST) filters are from the JADES program (M. J. Rieke et al. 2023). All filters have a pixel scale of 0.″03. The LyC flux in F435W, at 5.2σ significance, is clearly visible.

with a power law used to denote the redshift evolution of the CDDF. Extrapolating this redshift evolution to $z > 4$ may not produce accurate results, as IGM conditions are expected to change close to the EoR. The CDDF also becomes more difficult to measure at low column densities toward higher redshifts, as individual absorbers become more difficult to resolve in the Lyα "jungle" (R. M. Bielby et al. 2020). This is particularly important as the IGM transmission mostly depends on the prevalence of lower-column-density absorbers, i.e., the incidence rate of high-column-density Lyman limit systems (or LLSs) along the line of sight will determine the absorption of LyC photons (A. K. Inoue et al. 2014). We also note that this simulation does not include the effects of large-scale structure, which may result in a systematic bias in the estimated value of $T_{\rm IGM}$ (C. M. Scarlata et al. 2025).

An estimate of the Lyα transmission in the MXDF, at an impact parameter of $\sim$100 kpc from MXDFz4.4, already exists (J. Matthee et al. 2024). The authors find a Lyα transmission of 0.292 ± 0.008 at $z = 4.46$ using the absorption spectrum of a bright LAE at $z = 4.77$, making this more transmissive than typical quasar sight lines at this redshift. We take the transmission spectrum of this LAE (MUSE ID 53) and attempt to derive a LyC transmission from it. We obtain 0.05 ± 0.03, which is higher than the average transmissive sight line expected at $z = 4.44$. However, the spectral resolution of quasar spectra normally used to study H I gas at these redshifts is a factor of $\sim$10 greater than that of MUSE (G. D. Becker et al. 2015; R. M. Bielby et al. 2020; E. K. Lofthouse et al. 2020). Additionally, quasar spectra generally have much higher SNR. We therefore cannot determine the H I column density with sufficient accuracy to reliably constrain the LyC transmission. Furthermore, the correlation between the sight lines to MUSE ID 53 and MXDFz4.4 may be poor due to the impact of CGM-scale absorbers, which can have a large

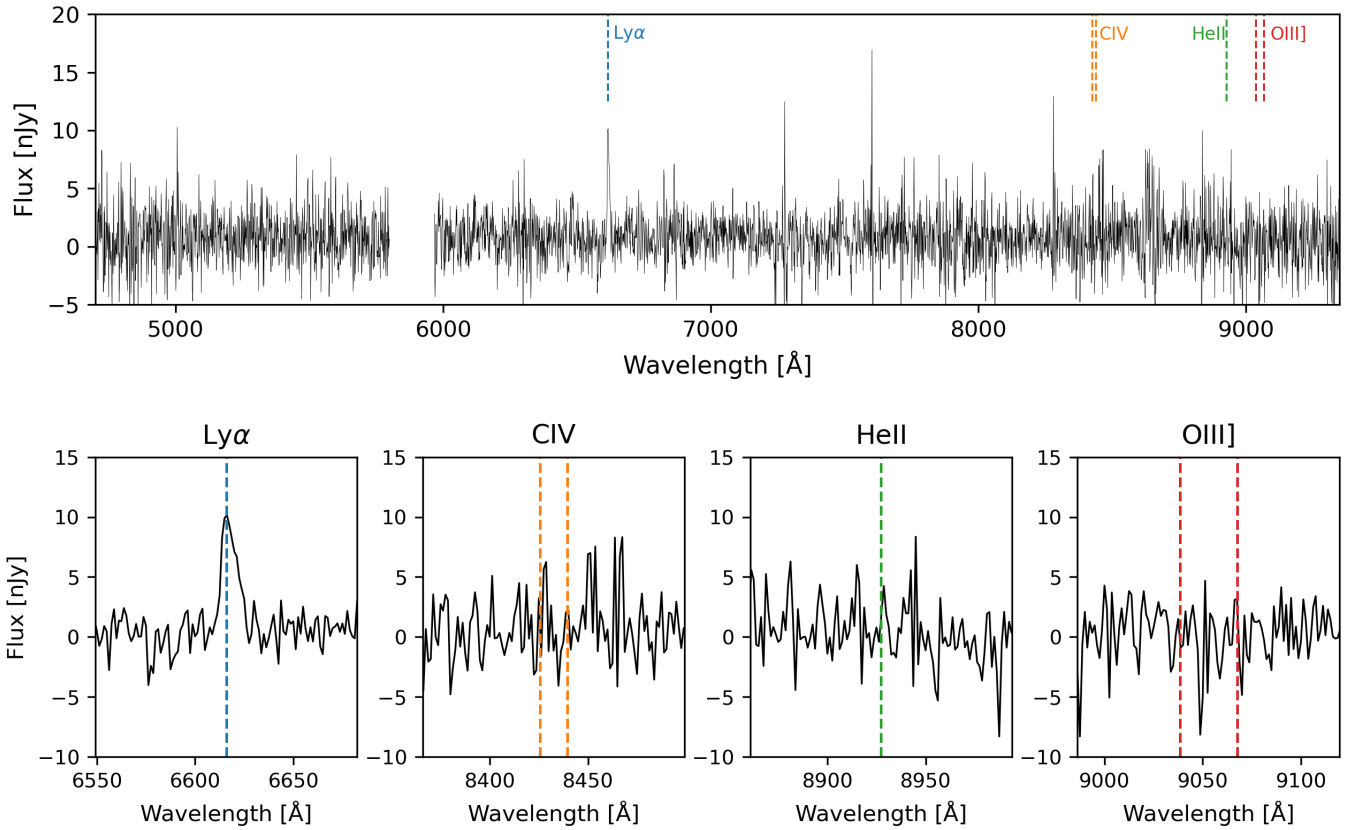

Figure 4. MUSE spectrum of MXDFz4.4. Cutouts of the UV lines are shown enlarged below the main spectrum. The Lyα line at 6615.9 Å is evident from its asymmetric line shape. No other emission lines are detected in the MUSE spectrum.

impact on the LyC transmission (e.g., G. C. Rudie et al. 2013; A. K. Inoue et al. 2014). We therefore choose not to trust this derivation of $T_{\rm IGM}$ and rely on the modeling previously described in this section.

4. The Escape Fraction of MXDFz4.4

In this section we start by defining the terms used in the explanation and calculation of the LyC escape fraction. This is followed by the measured and derived quantities for MXDFz4.4.

4.1. Escape Fraction Definitions

The observed flux ratio between the photometric bands that measure the flux blueward of 912 Å (LyC flux) and the UV flux is denoted by $f_{\rm LyC}/f_{\rm UV}$. This contains no model assumptions and is purely an observed quantity. However, the effect of the absorption by the IGM is not taken into account, nor is the intrinsic ratio between the ionizing and nonionizing flux. These quantities are captured in the relative escape fraction (C. C. Steidel et al. 2001; B. Siana et al. 2007):

$$f_{\rm esc,rel} = \left(\frac{f_{\rm LyC}}{f_{\rm UV}}\right)_{\rm observed} \left(\frac{L_{\rm UV}}{L_{\rm LyC}}\right)_{\rm intrinsic} e^{\tau_{\rm IGM}}. \quad (1)$$

We note that the exponential factor at the end of this expression is equal to $\mathbf{1/}T_{\rm IGM}$; $T_{\rm IGM}$ is plotted in Figure 7. Both this and the UV-to-ionizing luminosity ratio are model-dependent quantities, the first derived by the TAOIST modeling (Section 3.2) and the second by our SED fitting (Section 3.1).

Typically, a further quantity is defined to account for the effect of absorption by dust in the galaxy, termed the absolute escape fraction:

$$f^{\rm IGM}_{\rm esc,abs} = f_{\rm esc,rel} \times 10^{-0.4A_{\rm v}}, \quad (2)$$

where $A_{\rm v}$ is the dust attenuation in the rest-frame UV, another model-dependent quantity. We mark this quantity with the superscript IGM to denote that it is corrected for IGM absorption.

We present two methods of deriving MXDFz4.4's escape fraction. The first assumes an intrinsic luminosity ratio in Equation (1), which comes from stellar population modeling, and then we correct for dust using Equation (2). We adopt an intrinsic luminosity ratio of 3, common in the literature (C. C. Steidel et al. 2001; J. Kerutt et al. 2024), and a range of 1.0–1.5 based on our young, metal-poor pySTARBURST99 models (Figure 6). The second method derives the luminosity ratio directly from the CIGALE best-fit models (see Section 3.1 and Table 1), which already takes dust attenuation into account, hence yielding $f^{\rm IGM}_{\rm esc,abs}$ directly.

4.2. Escape Fraction Derivations

We start by considering luminosity ratios derived by CIGALE in Equation (1). For the third term in Equation (1), going forward we consider that the MXDF is a sight line that has a transmission 3σ above the mean simulated transmission: $T_{\rm IGM} \sim 0.18$ (see Section 3.2). We discuss this assumption in

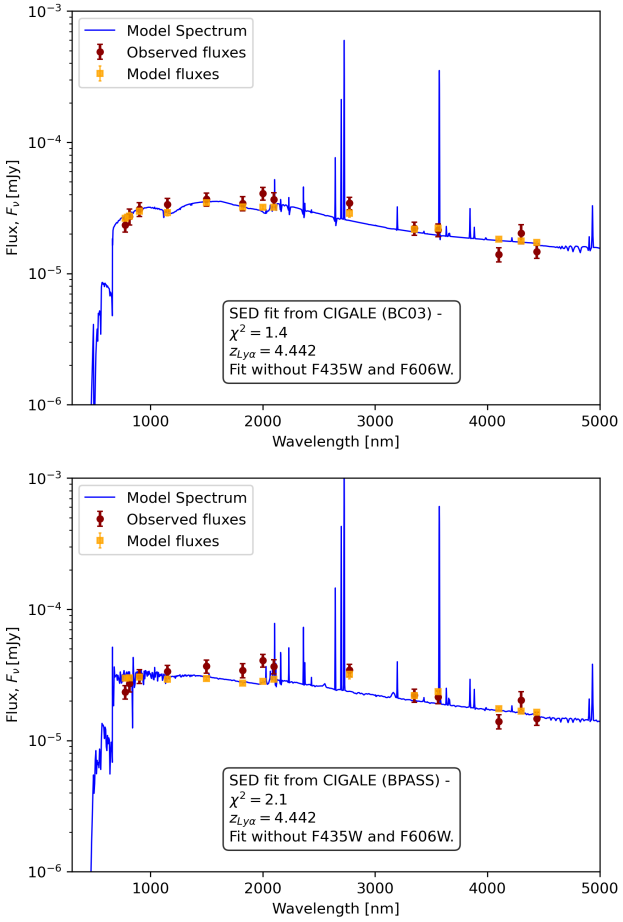

Figure 5. The best-fitting spectra of MXDFz4.4 obtained with CIGALE using the BC03 and BPASS stellar population models (G. Bruzual & S. Charlot 2003; J. J. Eldridge et al. 2017), plotted in blue. The observations are overplotted in red and the model fluxes in orange. The fit was performed without the F435W and F606W bands in order to predict the fluxes in the IGM-affected bands and derive $L_{1500}/L_{\rm LyC}$. The redshift was fixed to the value of $z = 4.442$, as derived from the Lyα emission line.

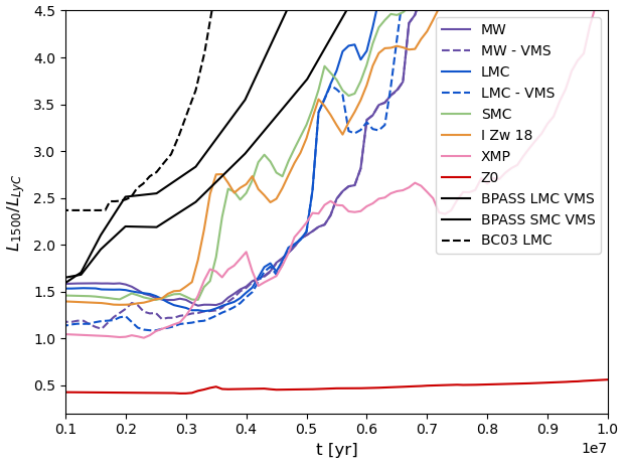

Figure 6. Evolution of $L_{1500}/L_{\rm LyC}$ over the first 10 Myr of a starburst, based on the pySTARBURST99 models (C. Hawcroft et al. 2025; in color), as well as the BPASS (J. J. Eldridge et al. 2008, 2017) and BC03 (G. Bruzual & S. Charlot 2003; in black) models. Values have been convolved with the F435W and F775W transmission curves and are expressed in F_ν to enable comparison with the observations. Metallicities range from Milky Way metallicity ($Z \sim 0.14$) to extremely metal-poor (XMP; $Z \sim 10^{-5}$), with a zero-metallicity line included for reference. VMS indicates models that include very massive stars with masses up to 300 $M_\odot$.

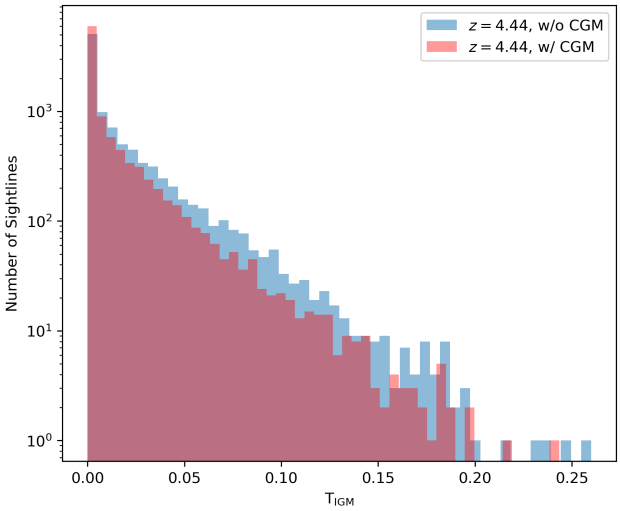

Figure 7. The IGM transmission (defined as $e^{\tau_{\rm IGM}}$) through F435W at the redshift of MXDFz4.4, based on 10,000 mock sight lines modeled using the TAOIST code as described in Section 3.2. We show the results including and excluding the CGM of MXDFz4.4.

Section 6. Using the observed flux ratio of 0.18 ± 0.04, we calculate $f_{\rm esc,abs}^{\rm IGM}$ values of 100% ± 32% (BC03) and 100%–120% (BPASS).

Using a luminosity ratio of 3 and the attenuation derived by our SED fitting, we obtain a $f_{\rm esc,rel}$ of 300% and a possible $f_{esc,abs}^{\rm IGM}$ range of 160%–220%. As this results in an escape fraction $\gg$100%, we consider it unlikely that the intrinsic luminosity ratio in MXDFz4.4 is as high as 3. This is further discussed in Section 6.

The luminosity ratios derived from the BPASS and pySTARBURST99 models (C. Hawcroft et al. 2025) are shown in Figure 6. Given the recent burst in star formation shown by our models and the necessity for $f_{\rm esc}$ to be <100%, we focus on the low-$L_{1500}/L_{\rm LyC}$ end of the range shown. As the $L_{1500}/L_{\rm LyC}$ value derived from CIGALE is also low, this plot is useful to visualize the possible nature of the recent burst in MXDFz4.4. The luminosity ratio range we consider from the young pySTARBURST99 stellar models is 1.0–1.5, which captures the low-metallicity stellar populations at an age of $\lesssim$5 Myr. This gives an $f_{\rm esc,rel}$ range of 100%–150% and an $f_{\rm esc,abs}^{\rm IGM}$ range of 53%–109%.

As an escape fraction of >100% is unphysical, either $L_{1500}/L_{\rm LyC}$ must be below a certain value or our result invokes a tension with the IGM models described in the previous section. We consider a lower bound of 53%, as given using the luminosity ratios from the pySTARBURST99 models. While a range of $f_{\rm esc}$ = 53%–100% is large in absolute terms, this reflects the uncertainty surrounding the model assumptions inherent to the $f_{\rm esc}$ calculation at high redshift, where we do not know the intrinsic ratio of ionizing to UV photons or the exact opacity of the IGM. Moreover, the small number of LCEs in the literature within this range are classed as strong LCEs, making a comparison with MXDFz4.4 useful. We now move on to comparing the properties of MXDFz4.4 to other objects in the literature and $f_{\rm esc}$ tracers established at low redshift.

Table 2
MXDFz4.4 Lyα Properties

Property	Value
MUSE ID	280
R.A.	53.1577218
Decl.	−27.7822649
Flux	$93 \pm 8 \times 10^{-20}$ erg s cm^{-2}
Luminosity	$1.8 \pm 0.2 \times 10^{41}$ erg s^{-1}
EW	17 ± 2 Å
FWHM	405 ± 52 km s^{-1}
Red peak asymmetry	2.1 ± 0.6
$r_{50,\mathrm{Ly}\alpha}$	$2.4^{+0.6}_{-0.5}$ kpc
$f_{\mathrm{esc,Ly}\alpha}$	2%–7%,[a] 5%–55%,[b] 13% ± 2%[c]
Halo fraction	$0.27^{+0.15}_{-0.18}$

Notes.
[a] Using SFR derived from CIGALE using BC03 models.
[b] Using SFR derived from CIGALE using BPASS models. The range comes from the range of SFRs derived in different runs (see Section 3.1).
[c] Derived using UV magnitude observed in the F775W filter.

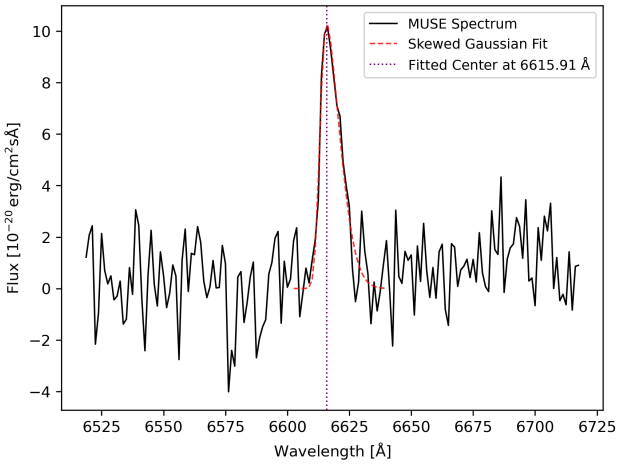

Figure 8. A zoom in on MXDFz4.4's Lyα emission line. The skewed-Gaussian fit to the line, described in Section 5.1.1, is plotted in red, and the fitted peak of the line at 6615.91 Å is plotted in purple. The properties of the line derived from the fit are detailed in Table 2.

5. Evaluating f_{esc} Tracers

MXDFz4.4 represents a significant step forward in measuring the properties of the LCEs actually responsible for the reionization process, as it is ∼35 times closer to the end of the EoR (in terms of time elapsed) than low-redshift studies (S. R. Flury et al. 2022a; A. E. Jaskot 2025) and a factor of 3–4 less than the time between the end of the EoR and $z \sim 3$–3.5, where previous high-redshift f_{esc} studies based on multiple galaxies have been focused (C. C. Steidel et al. 2018; A. J. Pahl et al. 2021; T. E. Rivera-Thorsen et al. 2022; A. Beckett et al. 2025).

First, we focus on the important Lyα–LyC connection, taking full advantage of MUSE's spectral resolution and spatial information. In the following sections, we also connect the SFR surface density, Σ_{SFR}, and the UV slope with f_{esc}.

As mentioned in the previous section, we consider in our analysis an envelope of possible escape fractions, 53%–100%, ranging from the minimum value (based on $L_{1500}/L_{\mathrm{LyC}}$ ratios) to the maximum possible value implied by our IGM transmission corrections. While this is a large range in absolute terms, there are few LCEs observed in the local Universe with $f_{\mathrm{esc}} > 50\%$, hence it remains useful to compare MXDFz4.4's properties with those LCEs of high escape fraction that have been observed.

5.1. The Lyα–LyC Connection

Thanks to the integral field unit data of MXDFz4.4 from MUSE, we have full access to both spectral and spatial Lyα tracers of f_{esc}. We start by comparing MXDFz4.4's Lyα properties to low-redshift predictions. A summary of all the relevant properties is given in Table 2.

5.1.1. Lyα Emission-line Properties

The simplest Lyα properties we can study are the flux and the EW. In order to derive the Lyα flux (see Figure 8), we perform a custom skewed-Gaussian fit to the line, closely following the procedure in R. Bacon et al. (2023). The skewed-Gaussian equation we fit is as follows:

$$F(\lambda) = A\left[1 + \mathrm{erf}\left(\frac{\gamma\,(\lambda - \lambda_0)}{\sqrt{2}\,\sigma}\right)\right]\exp\left(-\frac{(\lambda - \lambda_0)^2}{2\sigma^2}\right), \quad (3)$$

where A is the amplitude of the Gaussian, λ_0 is the central wavelength, σ is the standard deviation, and γ is the asymmetry parameter, large positive γ in this case leading to a more redward-skewed line. The flux of this line is calculated in the same way as a normal Gaussian function:

$$F_{\mathrm{tot}} = \int_{-\infty}^{\infty} F(\lambda)\,d\lambda = A\,\sigma\,\sqrt{2\pi}. \quad (4)$$

We subtract the background from this flux measured in two representative windows of 66.25 Å (53 MUSE spectral pixels) around the emission line. We subtract the median pixel flux in these two windows multiplied by the number of pixels underneath the Lyα line. The final Lyα flux is $93 \pm 8 \times 10^{-20}$ erg s cm^{-2}. This is completely consistent with the value from the public MXDF catalog (R. Bacon et al. 2023). As there is no continuum detected in the MUSE data, we then calculate the Lyα EW by taking the ratio of the Lyα flux to the flux in the F606W filter, which contains the 1216 Å emission, having first subtracted the Lyα flux from this filter. The result is an observed Lyα EW of 95 ± 11 Å, which gives a rest-frame EW of 17 ± 2 Å.

We compare this Lyα EW with literature results in Figure 9, where we shade in red the full region that MXDFz4.4 could occupy in terms of f_{esc} and $\pm 1\sigma$ in terms of Lyα EW. This region is outside the range of results from low redshift (S. R. Flury et al. 2022b), although there is significant scatter (gray points). However, this region is also in significant disagreement with the relation at high redshift established by A. J. Pahl et al. (2021). That said, the Lyα EW is not expected to be a good tracer at very high f_{esc}. This stems from the necessary reduction in nebular emission when a high fraction of ionizing photons escape the galaxy rather than powering the nebular emission from the ISM.

While the Lyα escape fraction is generally closely related to the EW (D. Sobral & J. Matthee 2019; R. Begley et al. 2024;

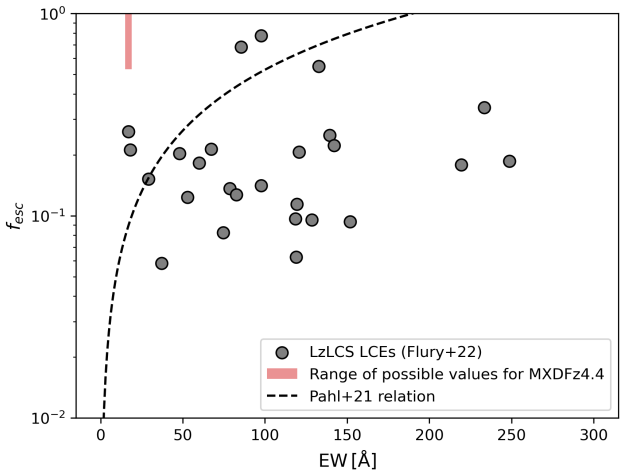

Figure 9. Lyα EW vs. f_{esc}, with the range of possible values for MXDFz4.4 highlighted in light red. The darker red area denotes the range derived using the L_{1500}/L_{LyC} value from CIGALE. The literature results (gray points) are collected by S. R. Flury et al. (2022b; low z) and the dashed relation is from A. J. Pahl et al. (2021; high z). The red area representing MXDFz4.4 has a width of $\pm 1\sigma$ in Lyα EW and the full range of possible values for f_{esc}: 27%–100%.

I. Goovaerts et al. 2024), it should scale with f_{esc} even to high f_{esc} values if the $f_{esc,Ly\alpha}$ is calculated using nonresonant hydrogen lines, such as Hα. Indeed, a close relation between f_{esc} and $f_{esc,Ly\alpha}$ has been found (S. R. Flury et al. 2022b; A. E. Jaskot et al. 2024; A. E. Jaskot 2025). However, as we do not have access to these lines for MXDFz4.4, we resort to comparing f_{esc} to $f_{esc,Ly\alpha}$ calculated using our SED fitting and the UV magnitude in the F775W filter.

We calculate the $f_{esc,Ly\alpha}$ using the dust-corrected SFRs from our CIGALE runs. Because the SFR has evolved dramatically over the last 100 Myr—and even likely over the last 10 Myr as our SED fitting suggests—we consider both averaged SFR values (see Table 1). In the past, Lyα escape has been calculated using both UV-derived SFRs and Hα-derived SFRs. Our results for the 100 Myr-averaged SFRs can be more readily compared with the UV-based method, and our 10 Myr results with the Hα method. We therefore give a range of possible $f_{esc,Ly\alpha}$ values in Table 2 (individual uncertainties are far smaller than the range) for the BC03 models, the BPASS models, and also for a comparison to the value derived using the UV magnitude simply converted to an SFR following the standard prescription from R. C. Kennicutt (1998). We caution that this prescription assumes a constant SFR over longer than 100 Myr, which is very unlikely to be the case for MXDFz4.4. The Lyα escape fractions derived are 2%–7% (BC03), 5%–55% (BPASS), and 13% $\pm$ 2% (UV magnitude). Because of the numerous assumptions and model dependencies used to obtain these values, it is challenging to meaningfully interpret them alongside low-redshift results. They vary from quite low, given that MXDFz4.4 is a strong LCE, to quite high. Observations of the Hα line would be necessary to more reliably determine the MXDFz4.4's SFR and therefore $f_{esc,Ly\alpha}$. However, if it is indeed the case that MXDFz4.4 is a very strong LCE, observing its accordingly reduced Hα emission may be challenging.

The asymmetry of the Lyα line is generally thought of as resulting from kinematics in the neutral gas in the ISM and CGM, such as outflows, as well as back-scattering. K. Kakiichi & M. Gronke (2021) suggest that galaxies with their ISM in the density-bounded scenario (in which ionizing photons escape) have a lower red peak asymmetry (i.e., a more symmetric line). Thus, this quantity may provide a simple way to assess the porosity of the ISM, crucial for allowing LyC escape. This is tentatively borne out in the observational sample of Y. I. Izotov et al. (2016, 2018a, 2018b). We define the red peak asymmetry, A_f, similarly to K. Kakiichi & M. Gronke (2021):

$$A_f = \frac{\int_{\lambda_{\mathrm{red\ peak}}}^{\infty} f_\lambda \, d\lambda}{\int_{\lambda_{\mathrm{valley}}}^{\lambda_{\mathrm{red\ peak}}} f_\lambda \, d\lambda}, \tag{5}$$

where f_λ is the Lyα flux, $\lambda_{\mathrm{redpeak}}$ is the wavelength at the red peak, and $\lambda_{\mathrm{valley}}$ is the wavelength between the red and blue peaks. In this case there is no blue peak, so we take a wavelength 20 Å blueward of the red peak. The resulting A_f is robust to this choice of lower integration limit. We calculate A_f to be 2.1 $\pm$ 0.6, with an uncertainty calculated by Monte Carlo sampling (Equation (5)) within the 1σ limits of our skewed-Gaussian fit to the Lyα line. This is a low red peak asymmetry according to K. Kakiichi & M. Gronke (2021), consistent with the galaxies they find to be strong LCEs, with mostly density-bounded ISM conditions.

The FWHM of the Lyα line is, however, in light contradiction with expectations. A. Verhamme et al. (2015) showed that LAEs with narrow peaks, close to the systemic redshift, are good candidates to be LCEs. However, MXDFz4.4 has a relatively large FWHM: 405 $\pm$ 52 km s^{-1} (corrected for the MUSE line-spread function). Larger FWHM values generally indicate higher neutral hydrogen column densities. However, J. Kerutt et al. (2024) also find reasonably high FWHM values for 12 LCE candidates at $z > 3$, some of which are consistent with MXDFz4.4.

These slightly conflicting results for the spectral properties of MXDFz4.4's Lyα emission stress the need to also take into account its spatial properties. We do so in the following sections.

5.1.2. Lyα Halo Fraction

The Lyα HF is currently a very promising tracer of f_{esc} at low redshift (J. Puschnig et al. 2017; A. Saldana-Lopez et al. 2026). Broadly, it encapsulates the amount of Lyα emission that escapes the host galaxy in an extended halo, rather than cospatially with the UV emission. A low HF indicates the presence of clear channels in the ISM and CGM of the galaxy through which Lyα photons escape with minimal scattering events, facilitating LyC photon escape. A. Saldana-Lopez et al. (2026) fit a relation between the HF and f_{esc} of $\log_{10}(f_{esc}) = (-2.32 \pm 0.41) \times \mathrm{HF} - (0.38 \pm 0.25)$ at low redshift from the Lyman Alpha and Continuum Origins Survey (LaCOS; A. Le Reste et al. 2025). We study this quantity, and its relation to f_{esc}, for the first time at high redshift.

In order to compute the HF for our data, where the Lyα comes from MUSE and the UV continuum comes from HST's F775W filter, we broadly follow the method laid out by L. Wisotzki et al. (2016) and close to that employed by A. Saldana-Lopez et al. (2026) to facilitate comparison. The key differences between our available data and those of

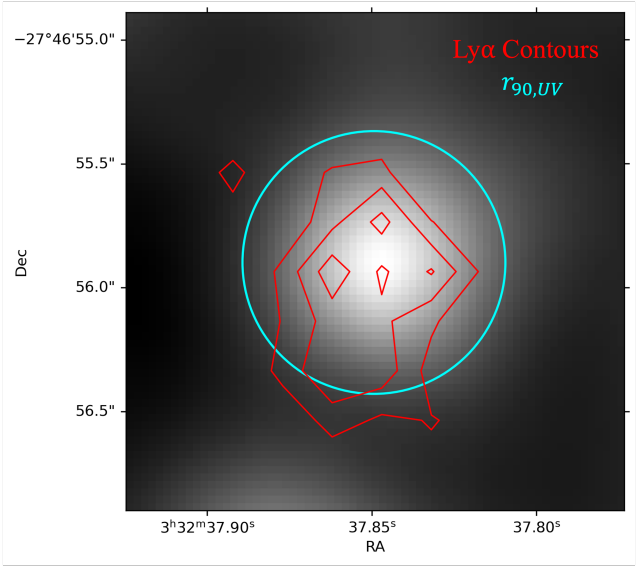

Figure 10. 2σ, 3σ, 4σ, and 5σ contours of Lyα (red) shown over the F775W image, which traces the rest-frame UV emission, PSF-matched to MUSE. The cyan circle denotes $r_{90,\mathrm{UV}}$.

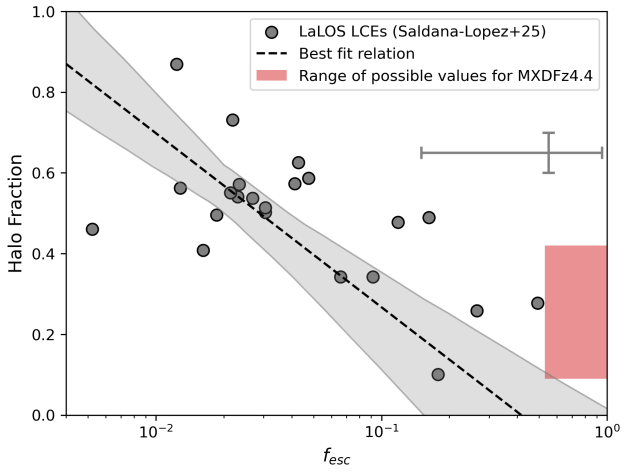

Figure 11. The Lyα halo fraction (HF) vs. f_{esc}. Gray points, representative error bars, and the best-fit relation are taken from the LaCOS sample in A. Saldana-Lopez et al. (2026). The range of possible values for MXDFz4.4 is highlighted as in Figure 9.

A. Saldana-Lopez et al. (2026) are that Lyα is detected in MUSE rather than HST and that no continuum is detected in Lyα. Thus, we must combine the two datasets to calculate the HF.

First, a narrowband (NB) image must be created around MXDFz4.4 from the MUSE datacube. We create the NB image for our HF calculation by summing the datacube in a 20 Å window around the wavelength of the Lyα emission, which contains all the Lyα flux. However, this NB image still has a much larger PSF than the HST image, so morphological comparisons are not yet possible. We therefore convolve the HST image to the MUSE PSF, using the Moffat profile described in R. Bacon et al. (2023) for the MXDF. Figure 10 shows the contours of Lyα emission overplotted on the UV emission from F775W, PSF-matched to MUSE. The $r_{90,\mathrm{UV}}$ is also shown for reference.

We then cut out a $3 \times 3''$ window around MXDFz4.4 and subtract the local background from each, masking MXDFz4.4 and nearby sources in the process. Nearby sources remain masked and radial profiles are calculated for both Lyα and UV. These radial profiles are then compared after normalizing the profile to the core of the Lyα profile. The extended Lyα emission over the UV profile is then considered the Lyα halo, and the fraction of the total emission that this constitutes is considered the HF.

Using this method, we derive a HF of $0.27^{+0.15}_{-0.18}$. The significant uncertainty on this value stems from the uncertainty on the Lyα profile. As the integrated SNR of the Lyα emission is only $\simeq 11\sigma$, the outskirts of the profile have low SNR. Another issue affects the center of the profile, caused by the size of the MUSE pixels, $0.''2$. In the inner few tenths of arcseconds of the Lyα profile, only a small number of pixels are considered, which raises the uncertainty. Both of these effects naturally stem from the MUSE data, and cannot be mitigated, save in a source with much higher SNR (ideally $\geqslant 30\sigma$ integrated).

We plot MXDFz4.4's HF on Figure 11, together with the results from the LaCOS survey (A. Saldana-Lopez et al. 2026). As before, we plot the $\pm 1\sigma$ area for the HF and the full range of possible escape fractions. This range is mostly outside the 1σ uncertainty on the relation established by A. Saldana-Lopez et al. (2026); MXDFz4.4 has a higher fraction of Lyα flux emitted in the halo than expected or, equivalently, a higher f_{esc} than expected based on its HF. We note that the next two strongest LCEs also lie above the relation and its uncertainty. A lack of very high-f_{esc} LCEs means that it is challenging to truly test this relation in the regime MXDFz4.4 occupies.

On the other hand, we show that it is possible to constrain (albeit with large uncertainties) very small HFs with MUSE and HST data, lending confidence, from a methodological standpoint, to the possibility of the application of the HF relation across the full range of f_{esc} at high redshift. We do expect large uncertainties to remain for MUSE LAEs of lower Lyα SNR ($\ll 30$).

Going forward, increased statistics (most likely coming from $z \sim 3$) will greatly benefit the assessment of whether the HF is a reliable tracer of LyC escape at high redshift.

5.1.3. Lyα r50

Additional Lyα morphological parameters have been suggested as f_{esc} tracers. The compactness of the Lyα emission can be expressed more simply than the HF, using $r_{50,\mathrm{Ly}\alpha}$. This has also been shown to be a potentially valuable tracer of f_{esc} (A. Saldana-Lopez et al. 2026), and one which does not rely on a detection of the continuum. More compact galaxies, therefore with lower $r_{50,\mathrm{Ly}\alpha}$, exhibit higher f_{esc} values. The suggested interpretation broadly follows the logic used to explain the correlation between the concentration of the UV starlight and f_{esc} (see the following Section). Additionally, as with the interpretation of the HF, Lyα escaping mostly centrally indicates clear channels through the ISM toward the observer, which also elevate f_{esc}.

We derive $r_{50,\mathrm{Ly}\alpha}$ for MXDFz4.4 via forward modeling of the same local background-subtracted NB image as for the HF. The intrinsic surface-brightness distribution is modeled as a Sérsic profile and convolved with the MUSE PSF (see Section 2). Parameters are inferred using Markov Chain Monte Carlo sampling with the `python` package `emcee` (D. Foreman-Mackey et al. 2013, 2019).

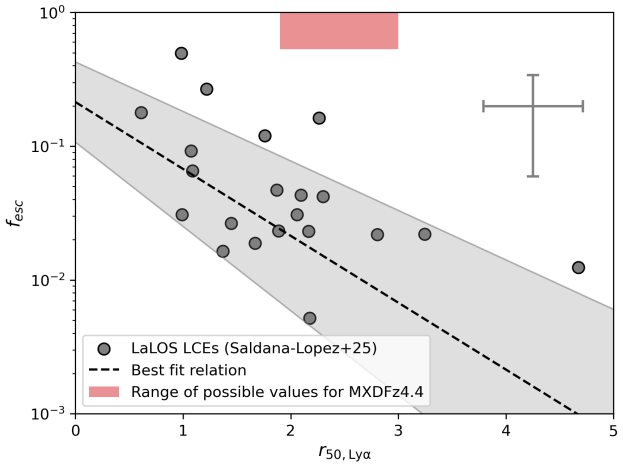

Figure 12. MXDFz4.4's $r_{50,Ly\alpha}$, plotted against its f_{esc}, compared to the sample of A. Saldana-Lopez et al. (2026) in gray. Colors denote the same as in Figures 9 and 11.

We find a MUSE PSF-adjusted $r_{50,Ly\alpha}$ value of $2.4^{+0.6}_{-0.5}$ kpc, which we plot as the red shaded area in Figure 12 together with the results from A. Saldana-Lopez et al. (2026), where once again this area encompasses the full range of possible f_{esc} values and $\pm1\sigma$ in $r_{50,Ly\alpha}$. We find less agreement here than in the HF, with the region demarcating MXDFz4.4 significantly outside the gray uncertainty region from A. Saldana-Lopez et al. (2026). However, we note that there are other LAEs of high f_{esc} that reside above this region, showing more extended Lyα emission than would be expected given their escape fractions.

Following a similar logic to $r_{50,Ly\alpha}$, the offset of the Lyα and UV centroids has also been suggested as a tracer of f_{esc} (A. Saldana-Lopez et al. 2026) through the $\Delta_{Ly\alpha-UV}/r_{90,UV}$ statistic. However, the value we measure is consistent with zero after accounting for uncertainties introduced by a potential, small World Coordinate System offset between F775W and MUSE. The offset matches expectations from comparing images of extremely different pixel sizes (10%–20% of the larger pixel size, in this case $0\farcs02 - 0\farcs04$) and the centroiding uncertainty itself, particularly for MXDFz4.4's clearly non-Gaussian profile. We therefore accept that it will always be challenging to extract significant conclusions from this statistic when combining MUSE and HST/JWST data.

5.2. Star Formation Rate Surface Density and Specific Star Formation Rate

A high SFR surface density, Σ_{SFR}, has been highlighted as a galaxy property that correlates with f_{esc} (Y. I. Izotov et al. 2016; S. Gazagnes et al. 2020; R. P. Naidu et al. 2020; A. E. Jaskot et al. 2024). The explanation centers on stellar feedback creating holes in the ISM more efficiently when the stellar environment is more concentrated (higher Σ_{SFR}).

We define Σ_{SFR} within MXDFz4.4's UV half-light radius using the typical equation for Σ_{SFR} (T. Shibuya et al. 2019; R. P. Naidu et al. 2020): $\Sigma_{SFR} = \frac{SFR/2}{\pi r_{50}}$. The half-light radius of MXDFz4.4 is $r_{50} = 0.63 \pm 0.04$ kpc, as derived in K. V. Nedkova et al. (2024) using a multiwavelength version of GALFIT (C. Y. Peng et al. 2002, 2010) that fits Sérsic profiles in all available filters simultaneously (B. Häußler et al. 2013). For MXDFz4.4, the 30 mas HST mosaics in nine filters were used to constrain the half-light radius: F435W, F606W, F775W, F814W, F850LP, F105W, F125W, F140W, and F160W. While the reprocessing of the ACS/WFC imaging as part of the HST archival program ID 16621 provide significant improvements to the image quality, these improvements are most significant in F435W and less so in F775W, the latter of which we use to measure the half-light radius. We therefore opt to use the results from K. V. Nedkova et al. (2024) that are constrained over multiple wavelengths, noting that we also find good agreement using the `photutils` package on the reprocessed F775W image, lending confidence to this result.

We derive a number of different SFRs for MXDFz4.4 (see Table 1) based on SED fitting and different timescales (10–100 Myr). The low end of these ranges gives Σ_{SFR} values less than $1\,M_\odot\,yr^{-1}\,kpc^{-2}$, which appears far too low for a strong LCE such as MXDFz4.4. The higher end of these ranges ($\gtrsim 10\,M_\odot\,yr^{-1}$) gives moderate Σ_{SFR} values around $5–6\,M_\odot\,yr^{-1}\,kpc^{-2}$. This is still not high considering the very high f_{esc} MXDFz4.4 likely exhibits. However, when looking in more detail at the SFH plots produced by `CIGALE`, the peaks of the recent burst (which is present in the SFH regardless of stellar population model choice) are around $9\,M_\odot\,yr^{-1}$ (BPASS) and $40\,M_\odot\,yr^{-1}$ (BC03). An SFR of $40\,M_\odot yr^{-1}$ gives a Σ_{SFR} value of $17\,M_\odot\,yr^{-1}\,kpc^{-2}$, which is more consistent with expectations for a strong LCE (A. E. Jaskot et al. 2024). However, such peak SFRs are not typically used for this calculation. The fact that MXDFz4.4 only has a Σ_{SFR} in line with low-redshift predictions when the peak of the recent starburst is considered is likely further evidence of the impact of this burst on the escape of LyC photons.

Although there is less of a correlation found between f_{esc} and specific star formation rate (sSFR; SFR divided by stellar mass), we note that most of the strong LzLCS LCEs have sSFR values above 10^{-8} (yr^{-1}), between 10^{-8} (yr^{-1}) and 10^{-7} (yr^{-1}) (S. R. Flury et al. 2022b). High f_{esc} in high-sSFR galaxies is also found in simulations (S. H. Menon et al. 2025). Using the same SFR ranges, and our `CIGALE` and BPASS-derived stellar mass of $10^{8.3}\,M_\odot$, we derive sSFR values between 1.2×10^{-8} (yr^{-1}) and 6×10^{-8} (yr^{-1}), consistent with the LCEs of very high f_{esc} in S. R. Flury et al. (2022b).

5.3. UV Slope

The UV slope, β, has been suggested as a promising tracer of f_{esc} at low redshift (J. Chisholm et al. 2022). It is particularly attractive as it is easy to measure at any redshift (albeit subject to uncertainties; e.g., D. Austin et al. 2025). The UV slope is sensitive to the dust content of the galaxy, as dust absorbs these UV photons and reemits them in the IR. The UV slope is additionally sensitive to the age and metallicity of the stellar population, with younger, metal-poor populations having bluer (more negative) slopes. However, nebular continuum emission from hot gas in the ISM created by such populations serves to redden the UV slope. It is argued that β is mainly sensitive to dust, implying that slope steepness should correlate with f_{esc}. This is indeed found at low redshift (J. Chisholm et al. 2022).

We fit the UV slope of MXDFz4.4 and find a redder slope than expected based on the relation found by J. Chisholm et al. (2022), both in the best-fit spectra from `CIGALE` and in the photometry. Avoiding the 2175 Å feature in the spectrum by calculating the slope in windows of 1250–1750 Å and 2400–2600 Å, we obtain a value using `CIGALE` and

the BC03 models of -1.6 ± 0.5. This is similar to the value derived using the observed photometry: $\beta = -1.4^{+0.3}_{-0.4}$. J. Chisholm et al. (2022) find that galaxies with very high $f_{\rm esc}$, such as MXDFz4.4 ($f_{\rm esc} \gtrsim 20\%$), mostly have $\beta < -2.6$. This suggests the presence of greater dust content than would be expected for a strong LCE, although the older, more chemically evolved component of the composite stellar population found by our SED fitting could also play a role in reddening the UV slope. We note that using the best-fit spectrum from CIGALE and BPASS gives a bluer slope (-1.9 ± 0.2), but that these fits fit the observed photometry slightly worse in the wavelength range where the UV slope is calculated (Figure 5).

We also caution that while the UV slope does depend on the dust attenuation along the line of sight—the same line of sight as the escape of LyC photons—it is far less impacted by morphology and the potential presence of clear channels in the ISM. The same applies to the escape of Lyα, as recently highlighted by V. Markov et al. (2026); T. Ejdetjärn et al. (2026). Different components of galaxies can contain differing amounts of dust and neutral hydrogen in their ISM, allowing LyC escape from only some parts of the galaxy. Hence, the integrated light of a galaxy may show the presence of dust, despite the existence of dust-clear channels through which LyC escapes (Z. Ji et al. 2025).

6. Discussion

In this section, we collect the measured properties of MXDFz4.4, as well as those that are dependent on models, discuss their validity, and infer the likely nature of MXDFz4.4.

Due to its very high redshift, and therefore the high opacity of the IGM, we conclude that MXDFz4.4's intrinsic escape fraction is very high, likely $\geqslant$50%. Given that an escape fraction of >100% is unphysical, we are left with two avenues to explain the detection of MXDFz4.4, based on Equation (1): Either the intrinsic luminosity ratio of nonionizing to ionizing photons (the second term) must be low or the transmission of the IGM must be low (the third term).

We consider the two cases from Table 1: using $L_{1500}/L_{\rm LyC}$ from stellar models (pySTARBURST and BPASS) and using $L_{1500}/L_{\rm LyC}$ directly from CIGALE (which includes dust). In the first case, (using the dust attenuation we derive with CIGALE in Equation (2)), the $L_{1500}/L_{\rm LyC}$ value must be $\leqslant$1.88 ($A_v = 0.68$) or $\leqslant$1.38 ($A_v = 0.34$). In either case, $L_{1500}/L_{\rm LyC}$ must be close to unity. This brings MXDFz4.4's observed $f_{\rm esc}$ into consistency with models of IGM transmission. For the CIGALE-derived case, $L_{1500}/L_{\rm LyC}$ must also be very near unity to avoid $f^{\rm IGM}_{\rm esc,abs} > 100$ %. As we can see from Figure 6, $L_{1500}/L_{\rm LyC}$ ratios of near unity are achieved only by very young and/or very metal-poor populations.

Even with such extreme stellar populations, only a small fraction of sight lines are transmissive enough to allow the $f_{\rm esc}$ that we observe from MXDFz4.4, according to our modeling (Section 3.2 and Figure 7). Using the stellar modeling approach (row 2 of Table 1), a $T_{\rm IGM}$ value of >10.4 is necessary to ensure $f^{\rm IGM}_{\rm esc,abs} < 100\%$ even with the best-case dust attenuation. This is satisfied by just over 2% of sight lines. Using the CIGALE approach (rows 3 and 4 of Table 1), this reduces to 0.3% of sight lines ($T_{\rm IGM} < 0.18$). This can be interpreted as a "3σ-unlikely sight line." The previous case, $T_{\rm IGM} > 10.4$, is equivalent to a little over 2σ unlikely.

It is possible that the IGM actually allows a greater transmission of ionizing photons than the TAOIST models predict. Although the H I CDDF used by TAOIST is redshift dependent, it is primarily calibrated using observations from the Keck Baryonic Structure Survey (KBSS; G. C. Rudie et al. 2013) at $2 \lesssim z \lesssim 3$, and may therefore be inaccurate close to the EoR. TAOIST and other Monte Carlo–based IGM codes also generally do not account for H I clustering, which can be due to large-scale structure (C. M. Scarlata et al. 2025). This could also increase the transmission of the most transparent sight lines and reduce the possible tension (K. Kakiichi et al. 2018).

However, given that we do observe ionizing escape from MXDFz4.4, and that a young and/or potentially very metal-poor stellar population can account for this, we now discuss its physical nature by combining all the $f_{\rm esc}$ tracers that we have analyzed and the physical conditions we have derived. We caution that comparisons to other LCE samples may be limited by the lack of sufficient LCEs of very high $f_{\rm esc}$ in the literature.

The Lyα EW is in significant disagreement both with results found at low redshift and at high redshift (A. J. Pahl et al. 2021; S. R. Flury et al. 2022b). However, this may be expected for an LCE of very high $f_{\rm esc}$, as MXDFz4.4 is likely to be. The strength of nebular lines is expected to decrease when significant amounts of ionizing photons escape, as these photons are no longer available to produce recombination lines like Lyα.

For this reason, $f_{\rm esc,Ly\alpha}$ is expected to correlate with $f_{\rm esc}$ up to very high values, provided that it is calculated using nonresonant hydrogen recombination lines, such as Hα. This is not the case for MXDFz4.4 and, given the difficulty in deriving precise SFRs using SED fitting, we are left with a large range of $f_{\rm esc,Ly\alpha}$ values, derived in a number of ways. High values, as would be expected, are included, but unfortunately our results are not very constraining and therefore are difficult to compare to others in the literature.

Considering the Lyα asymmetry and HF, these agree fairly well in that a low HF indicates a direct path for LyC photons to escape the galaxy toward the observer, and a symmetric line suggests a density-bounded scenario that also allows for high levels of escape.

The high FWHM, however, is less in line with expectations from simulations and from low-redshift observations, as this can indicate high neutral hydrogen column densities, which would impede LyC escape. These slightly contradictory Lyα properties may be explained by the effect of the recent burst combined with an older, more evolved population (which likely exists given the redder-than-expected UV slope). Lyα photons can take time to escape from the galaxy (e.g., J. M. Mas-Hesse et al. 2003). At stellar ages younger than ~2.5 Myr, Lyα struggles to escape from the molecular clouds surrounding stars (M. Hayes et al. 2007). Then, feedback from massive stars, winds, and the first supernovae, such as we expect in MXDFz4.4's recent burst, progressively clear the clouds and facilitates both Lyα and LyC escape (D. Rahner et al. 2017; M. Trebitsch et al. 2017; C. A. Carr et al. 2025; L. Komarova et al. 2025). If the burst in MXDFz4.4 is at this stage, rapid development of the emergent Lyα emission would be expected, with some component remaining from the older stellar population and its ISM.

If MXDFz4.4's Lyα line is close to the systemic redshift, which has been shown to correlate well with $f_{\rm esc}$

(A. Verhamme et al. 2015, 2017; S. R. Flury et al. 2022b), this may alleviate the unexpectedly high FWHM. It would mean that a significant fraction of Lyα photons would escape at the systemic redshift rather than undergoing an extensive radiative transfer process through surrounding neutral hydrogen. This would help to explain the high fraction of LyC photons that also escape. Unfortunately, we lack the additional lines in MXDFz4.4's spectrum to verify this.

Among all the Lyα-based tracers, we note that one of the most promising at low redshift, the HF, qualitatively agrees with predictions, which moderately increases the confidence in the possibility of using it at high redshift. Further confidence would necessitate testing the HF method for much larger samples, especially in the lower-f_{esc} regime where the HF relation from A. Saldana-Lopez et al. (2026) is more constrained. Samples of LCEs in the f_{esc} range of MXDFz4.4 are likely to remain small for the foreseeable future, although will remain desirable to better constrain the high-f_{esc} regime.

With these conclusions regarding the Lyα properties of MXDFz4.4 in mind, we suggest that its recent star formation activity and the nature of its burst are the driving forces behind its high observed escape fraction. This highlights the importance of Σ_{SFR} and sSFR as tracers. It may be for this reason that the Lyα HF still acts as a good tracer of f_{esc}, while for example the Lyα r_{50} is less in line with low-redshift findings (A. Saldana-Lopez et al. 2026); the HF is the most sensitive of the Lyα diagnostics to the holes created in the ISM for Lyα and LyC to escape. Still, the Σ_{SFR} is lower than expected for all but the peak of the recent star formation, which likely means that the nature of the stellar population also plays a significant role, i.e., a young, metal-poor stellar population producing many ionizing photons per UV photon. To illustrate the importance of this, we refer the reader to the earlier discussion about the necessity of L_{1500}/L_{LyC} being near unity (note that this keeps all other parameters, as well as the actual escape of LyC photons, the same). Even the upper bounds on the possible L_{1500}/L_{LyC} ratios we calculate are low compared to the average galaxy population, and are surpassed, according to Figure 6, for all but the most metal-poor stars in 6–7 Myr.

Therefore, it is likely that the very young and potentially metal-poor nature of the stellar population in MXDFz4.4's recent burst is contributing strongly to its observation as an LCE. This is supported by the recent local Universe work of T. Ejdetjärn et al. (2026), where LyC is boosted due to recent star formation and is not necessarily cospatial with Lyα, which the authors attribute to LyC and Lyα originating in different locations (i.e., stars versus the ISM). A poststarburst boost in the f_{esc} of a galaxy has been well studied, both in simulations (N. Y. Gnedin et al. 2008; H. Yajima et al. 2009; T. Kimm & R. Cen 2014; M. Trebitsch et al. 2017; J. Rosdahl et al. 2022; S. H. Menon et al. 2025) and in observations (C. A. Carr et al. 2025; S. R. Flury et al. 2025; L. Komarova et al. 2025), with these studies also commenting on the importance of young, metal-poor stars in this process.

The burstiness of early galaxies within the EoR has recently been invoked to explain the excess of UV-bright galaxies observed at very high redshifts (X. Shen et al. 2023; G. Sun et al. 2023; J. B. Muñoz et al. 2026). These galaxies have already been suggested as efficient ionizers (R. Endsley et al. 2023; C. Simmonds et al. 2024), mostly due to their enhanced ionizing photon production efficiency and a potential higher f_{esc} (R. Endsley et al. 2024; M. J. Hayes et al. 2025). Our interpretation of MXDFz4.4's properties supports this, and it also suggests that galaxies with successive strong bursts of star formation may also experience episodes of extremely high LyC production and f_{esc}. We caution that this is dependent on metallicity, since more enriched populations would produce fewer ionizing photons. This process is cumulative, with successive bursts producing more enriched populations and fewer ionizing photons. However, elevated Σ_{SFR} and sSFR during the burst may still facilitate high levels of escape. Such bursty galaxies are therefore strong candidates to emit a large share of the ionizing photons needed to reionize the IGM at early times.

If high-redshift galaxies have a duty cycle closer to one (i.e., they spend close to 100% of their time in the star-forming phase), it might provide a mechanism for EoR galaxies to emit enough ionizing photons into the IGM to create the reionization history that we observe, a similar argument to that presented in R. P. Naidu et al. (2020) for Σ_{SFR}. For this reionization history, the necessary escape fraction on a population level has generally been placed around 5% (S. L. Finkelstein et al. 2019), which is far greater than what we observe in the local Universe. The increased burstiness of high-redshift galaxies might therefore help alleviate this issue.

7. Summary and Conclusions

We present the detection of the highest-redshift LyC emitter to date, MXDFz4.4, at $z = 4.442$. This redshift is confirmed by a high-confidence Lyα line in extremely deep, 140 hr MUSE spectroscopy. We apply all available tracers established by studies at low redshift and conclude the following about the nature of MXDFz4.4:

1. Our SED fitting with `CIGALE` and two different stellar population models (Figure 5) suggests a very recent and vigorous burst of star formation, with numerous stellar models predicting a very low L_{1500}/L_{LyC} ratio at these young ages. This would mean that MXDFz4.4's observed escape fraction is not in tension with models of IGM transmission at $z = 4.44$.
2. MXDFz4.4's Lyα EW is low (Figure 9) in comparison to both low- and high-redshift studies from the literature. However, this may be explained by MXDFz4.4's very high escape fraction. When f_{esc} is very high, nebular emission, including Lyα, is expected to decrease as ionizing photons are escaping rather than being absorbed and reemitted as Lyα.
3. MXDFz4.4's Lyα escape fraction, $f_{esc,Ly\alpha}$, is challenging to constrain without the Hα emission line. We use SED fitting and MXDFz4.4's UV magnitude instead, finding a wide range of $f_{esc,Ly\alpha}$ values, ranging from low to >50%.
4. The Lyα shape and FWHM are in slight conflict, with the line being symmetric (as expected for a strong LCE) but with a large FWHM (unexpected given simulations). This may be alleviated by MXDFz4.4's Lyα line being close to the systemic redshift, shown to be important in facilitating LyC escape. However, we lack the other emission lines to assess this.
5. The Lyα half-light radius, $r_{50,Ly\alpha}$, is also larger than expected for high-f_{esc} galaxies, lying outside of the predicted range based on low-redshift results. Both this

and the Lyα line FWHM could be attributed to rapid evolution of the MXDFz4.4's Lyα emission due to its recent burst, some contribution from an older stellar population, and more chemically evolved parts of the galaxy.

6. We tested the promising HF tracer established by A. Saldana-Lopez et al. (2026) for the first time at high redshift and find qualitative agreement with low-redshift results, although MXDFz4.4 occupies a sparsely populated area of the parameter space. Nevertheless, our results support the use of this promising tracer for high-redshift f_{esc} studies and demonstrate how this can be achieved with MUSE data. These results also reinforce the importance of geometry and orientation/viewing angle in the observation of escaping LyC photons. Applying the HF method to more high-redshift LCEs is necessary to truly ascertain its validity toward the EoR and therefore the potential importance of the presence clear channels in the ISM and CGM that this tracer probes. In particular, more high-f_{esc} LAEs are needed to assess whether MXDFz4.4 is a typical or an outlier case.
7. Among MXDFz4.4's star formation properties, sSFR is elevated and Σ_{SFR} is moderate, rising to very elevated when we consider the peak SFR of the recent burst. Both of these point to the importance of the recent burst of star formation in clearing the ISM and facilitating LyC escape.
8. We find a redder UV slope, β, than expected: ~ -1.4 from photometry and ~ -1.5 to -1.9 from the best-fit `CIGALE` models. This indicates the presence of some dust in the galaxy and means it is likely we are observing the LyC escaping thanks to a specific ISM geometry, also likely due to feedback from the recent burst.

Based on these results, we suggest that galaxies in the early Universe, which have been shown to undergo multiple bursts of vigorous star formation, may also undergo successive periods of extremely high ionizing photon production and escape, although the production is likely also dependent on metallicity. While more work is needed to confirm this, the bursty nature of high-redshift galaxies may provide an explanation for the discrepancy between the low levels of f_{esc} observed among the general galaxy population at low redshift and the number needed to reionize the IGM.

While the detection and characterization of MXDFz4.4 shows MUSE to be an extremely useful instrument for high-redshift LCE investigation, we warn that the HF method will not work with all MUSE-detected LAEs, as a significant fraction (10%–30%, depending on the relative depths of the MUSE data and photometry) are undetected in the continuum (R. Bacon et al. 2023; I. Goovaerts et al. 2023). Still, the $r_{50,Ly\alpha}$ and all the line shape diagnostics would remain available, making MUSE an efficient instrument to quantify f_{esc} in LAEs up to $z \sim 6.5$, well into the end of the EoR.

Acknowledgments

Based on observations with the NASA/ESA Hubble Space Telescope obtained at the Space Telescope Science Institute, which is operated by the Association of Universities for Research in Astronomy, Incorporated, under NASA contract NAS5-26555. Support for Program number 16621 provided through a grant from the STScI under NASA contract NAS5-26555. M.J.H. is supported by the Swedish Research Council (Vetenskapsrådet) and is Fellow of the Knut and Alice Wallenberg Foundation.

Software: CIGALE (M. Boquien et al. 2019), pySTARBURST99 (C. Hawcroft et al. 2025), BPASS (J. J. Eldridge et al. 2008, 2017), BC03 (G. Bruzual & S. Charlot 2003), TAOIST (R. Bassett et al. 2021), `emcee` (D. Foreman-Mackey et al. 2013), `photutils` (L. Bradley et al. 2025).

Appendix A
Redshift Confidence

To confirm the redshift of MXDFz4.4, we carried out a number of tests, positing the alternative possibilities that the emission line seen in the MUSE spectrum at 6615.9 Å is not Lyα but instead the [O II] λ3727 doublet, the stronger of the two [O III] lines (5007 Å), Hα, and the C III] doublet. The first three cases are shown below in the cutouts in Figure 13, clearly showing the lack of the other expected lines in the spectra. In the case of [O II] and C III], we show plots of [O II] and C III] emitters from the MUSE database in Figures 14 and 15, clearly showing that both of these doublets are resolved at $\sim$6600 Å. It is therefore clear that none of these cases are plausible.

In the case of Hα, we do not see either [O III], [N II] or [S II]. Additionally, the line at 6615.9 Å is visibly skewed, common for Lyα but extremely uncommon for Hα. Finally, if this line was Hα, the redshift would be $z = 0.008$, and detections would be expected even in the shallower F336W, F275W, and F225W images (Figure 3) depending on the SED shape, all of which contain nondetections. Finally, the source's compact morphology is not consistent with a galaxy at $z = 0.008$.

If the line were to be the [O II] λ3727 doublet, we would expect it to be resolved at the spectral resolution of MUSE. We show the spectrum of an [O II] emitter at the same SNR ($\sim 11\sigma$) and wavelength and show that it is easily resolved (Figure 14). Additionally, neither [O III] nor Hβ is detected. Even in the case of a very low ionization state, where [O II] is expected to be stronger than [O III], for an 11σ[O II] detection we would expect a $>4\sigma$ detection of the stronger [O III] line (based on an [O III]/[O II] ratio of 0.5, typically found in metal-rich low-z galaxies).

If the line at 6615.9 Å were to be the stronger of the two [O III] lines, we would expect to detect the weaker line at 3–4σ as this line ratio is $\sim$3 (independent of astrophysical conditions in the galaxy). In addition to this, not one of Hα, Hβ, or [O II] is detected.

Finally, Figure 15 clearly shows that the C III]λ1907, 1909 doublet is resolved at the wavelength that Lyα is detected in MXDFz4.4's spectrum.

Together with the clearly asymmetric line profile, these cases show that there is high confidence in MXDFz4.4's Lyα line and therefore its redshift of $z = 4.442$.

A.1. Chance Alignment with a Low-redshift Interloper or Supernova

We also discuss the possibility of a chance alignment between a low-redshift galaxy and a background LAE, such that the continuum that we see, including the detection in F435W, does not actually come from the line emitter we observe in the MUSE spectrum. In order to assess this probability, we start with the number density of quiescent galaxies from G. B. Brammer et al.

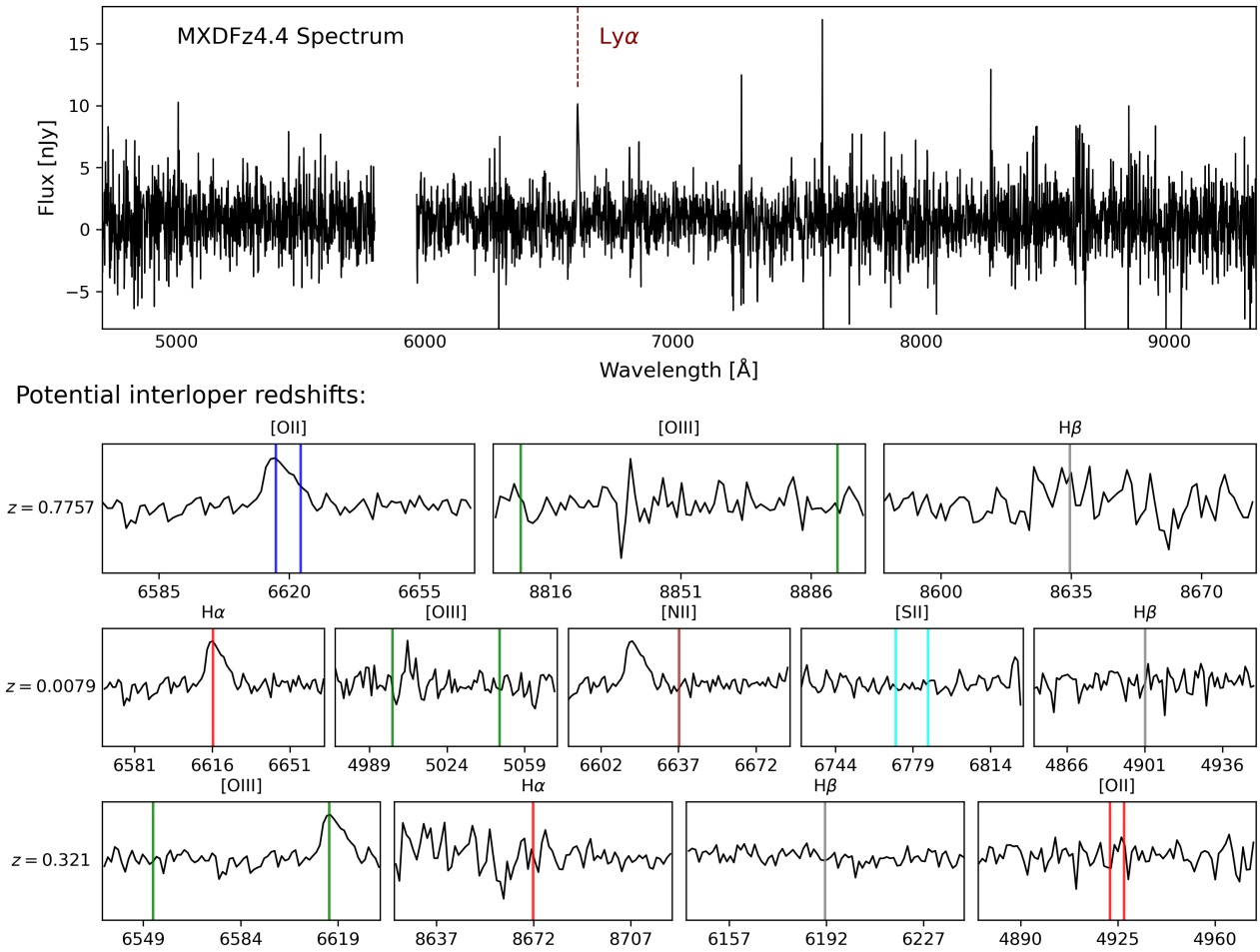

Figure 13. Testing potential interlopers for MXDFz4.4. We posit that the line at 6615.9 Å could be [O II], [O III], and Hα, and check for other lines at the corresponding redshifts. The top spectrum is the full MUSE spectrum of MXDFz4.4, each row of cutouts below represents a different interloper redshift, noted on the left. The first row plots the case of [O II] ($z = 0.7757$) and clearly shows the lack of [O III] or Hβ. The second row plots the case of Hα, where we see that [O III] and Hβ are not detected. The third row plots the case of [O III], where we show the blue [O III] peak is not detected, nor Hα, Hβ, or [O II]. These nondetections, combined with the clear asymmetry in the line at 6615.9 Å results in a high-redshift confidence for MXDFz4.4.

(2011): $\approx 7.3 \times 10^{-4}\,\mathrm{Mpc}^{-3}$ (lowest redshift and mass bin, as the SED is inconsistent with a very high-mass galaxy). The foreground galaxy must be quiescent, as it is not detected in the filters blueward of F435W, and no emission lines are detected in 140 hr-depth MUSE data. From this, we calculate the number of such galaxies that should exist in the MXDF in the 1σ interval of the JADES-derived photometric redshift: $0.391 < z < 0.476$, arriving at 0.039. As the alignment must be exact, we then compute the number of $0\farcs2$ circles (approximate centroid uncertainty between the two emissions, Lyα and continuum) that fit in the MXDF. This number, using Thue's circle-packing theorem (H.-C. Chang & L.-C. Wang 2010), is 20405. Combining this number with the 3.9% chance of the necessary galaxy existing in the MXDF field of view gives a chance of an alignment with any single LAE of 1 in 523,205. We multiply this by the number of LAEs in a feasible redshift range to detect LyC in F435W: $4.391 < z < 4.6$, yielding 40. This gives a final probability of a chance alignment producing the F435W flux we observe, of 1 in 13,080, or 0.0076 %.

We also rule out the possibility of the F435W flux that we detect being created by a supernova in a faint host galaxy which aligns with MXDFz4.4. This is done by showing the F435W is not a point source, but rather is extended and elongated. The F435W PSF FWHM is 3.4 pixels and the FWHM of MXDFz4.4's F435W flux is 5.3 pixels. The semimajor-to-semiminor axis ratio of MXDFz4.4 in F435W is 1.21, whereas for the PSF it is 1.01 (circular).

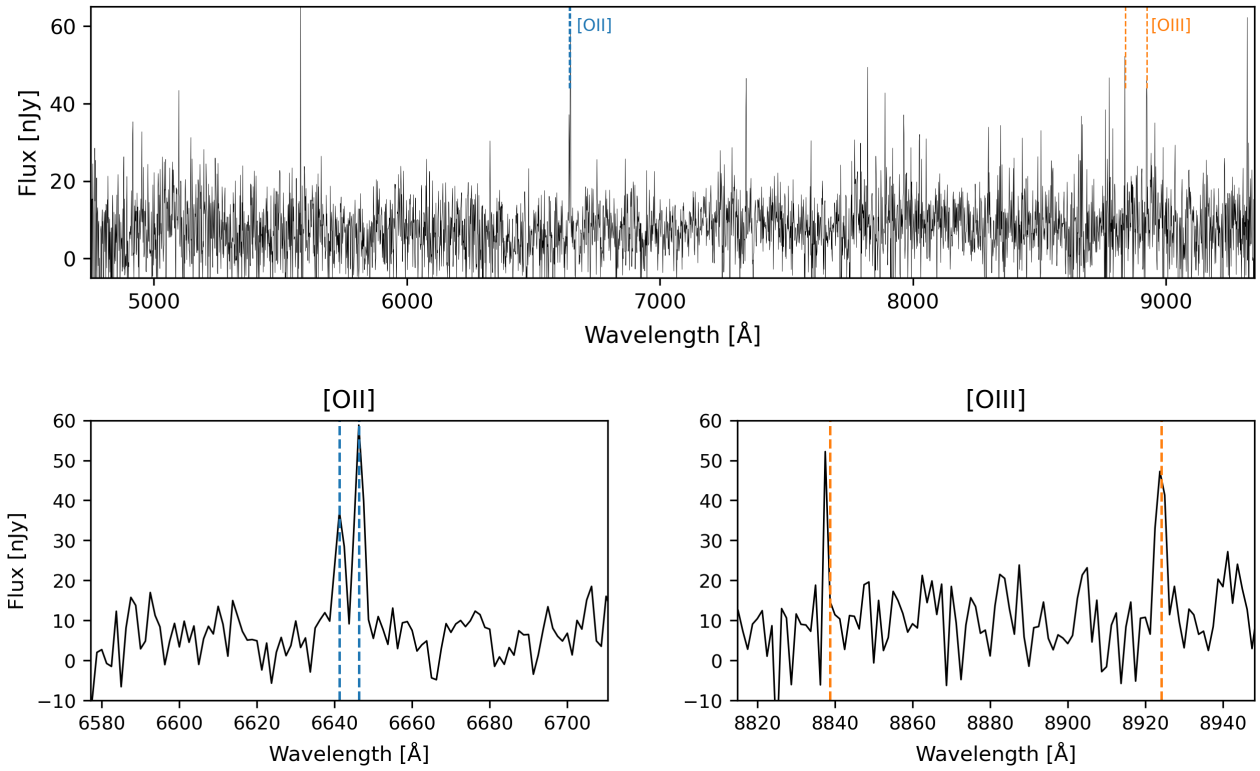

Figure 14. A spectrum of an [O II] emitter at a similar wavelength as MXDFz4.4's Lyα emission, and with a similar SNR ($\sim$10σ; MUSE object ID: 6969). The double peak is clearly resolved. Additionally, the [O III] doublet is clearly detected, while in MXDFz4.4's spectrum only one line is detected.

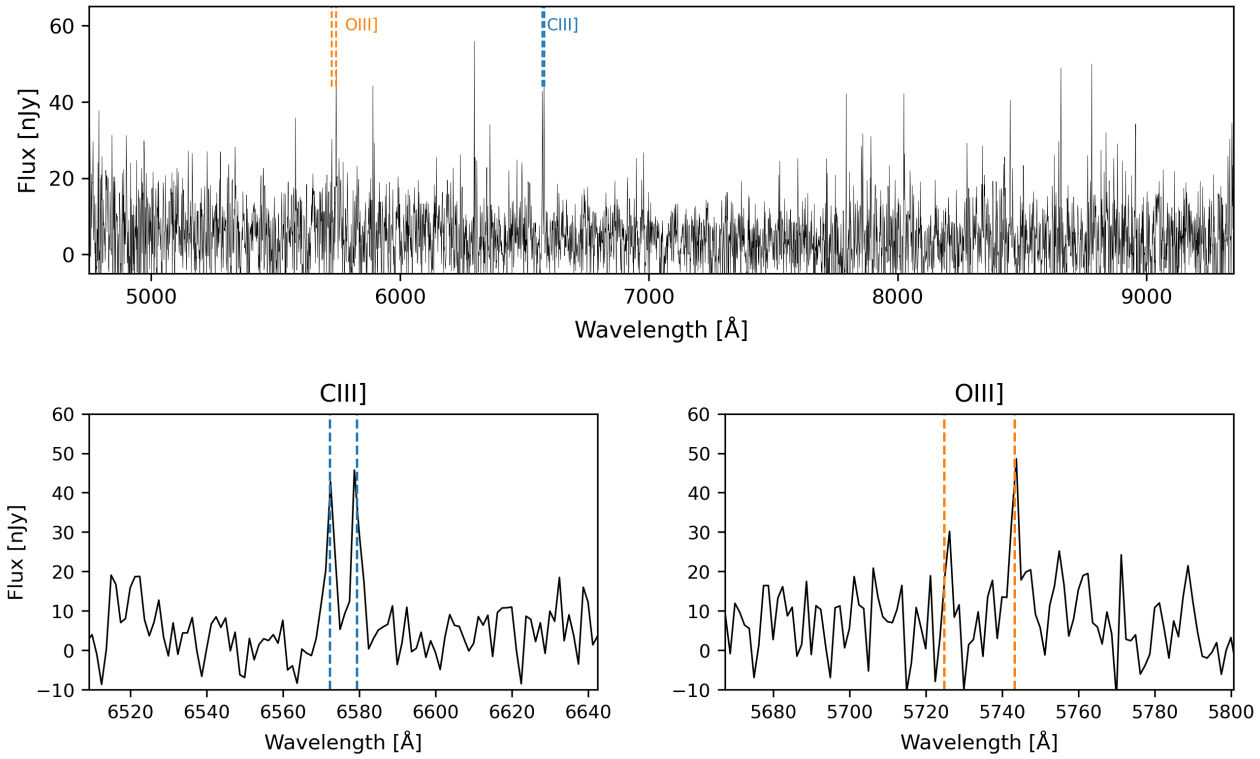

Figure 15. A spectrum of a C III]λ1907, 1909 emitter detected by MUSE, with C III] at a similar wavelength as MXDFz4.4's Lyα emission, and with a similar SNR ($\sim$7.5σ; MUSE ID: 1784). The double peak of C III] is clearly resolved. O III]λ1660, 1666 is also clearly detected in the spectrum.

Appendix B
JWST/NIRISS Spectrum of MXDFz4.4 from the NGDEEP Program

JWST/NIRISS wide-field slitless spectroscopy of the MXDF is available through the NGDEEP program (M. B. Bagley et al. 2024). We show this spectrum in Figure 16. There are no lines detected in MXDFz4.4's spectrum, despite NGDEEP's long exposure time in F200W of >31,000 s. However, considering the 5σ flux limit of the spectra, 1.2×10^{-18} erg s^{-1} cm^{-2} Å, it is unsurprising that no lines are detected. The strongest line that falls in the wavelength coverage of NIRISS is [O II] λ3727, which would fall at $\sim$2.03 μm. The 5σ limit of the spectrum is $\sim$30% more than the Lyα flux observed by MUSE, therefore it is not surprising that [O II] is not detected. There are even scenarios of Lyman photon escape, the density-bounded case (see, e.g., Figure 1 of A. E. Jaskot 2025), where [O II] is suppressed due to a lack of low-ionization gas in the ISM.

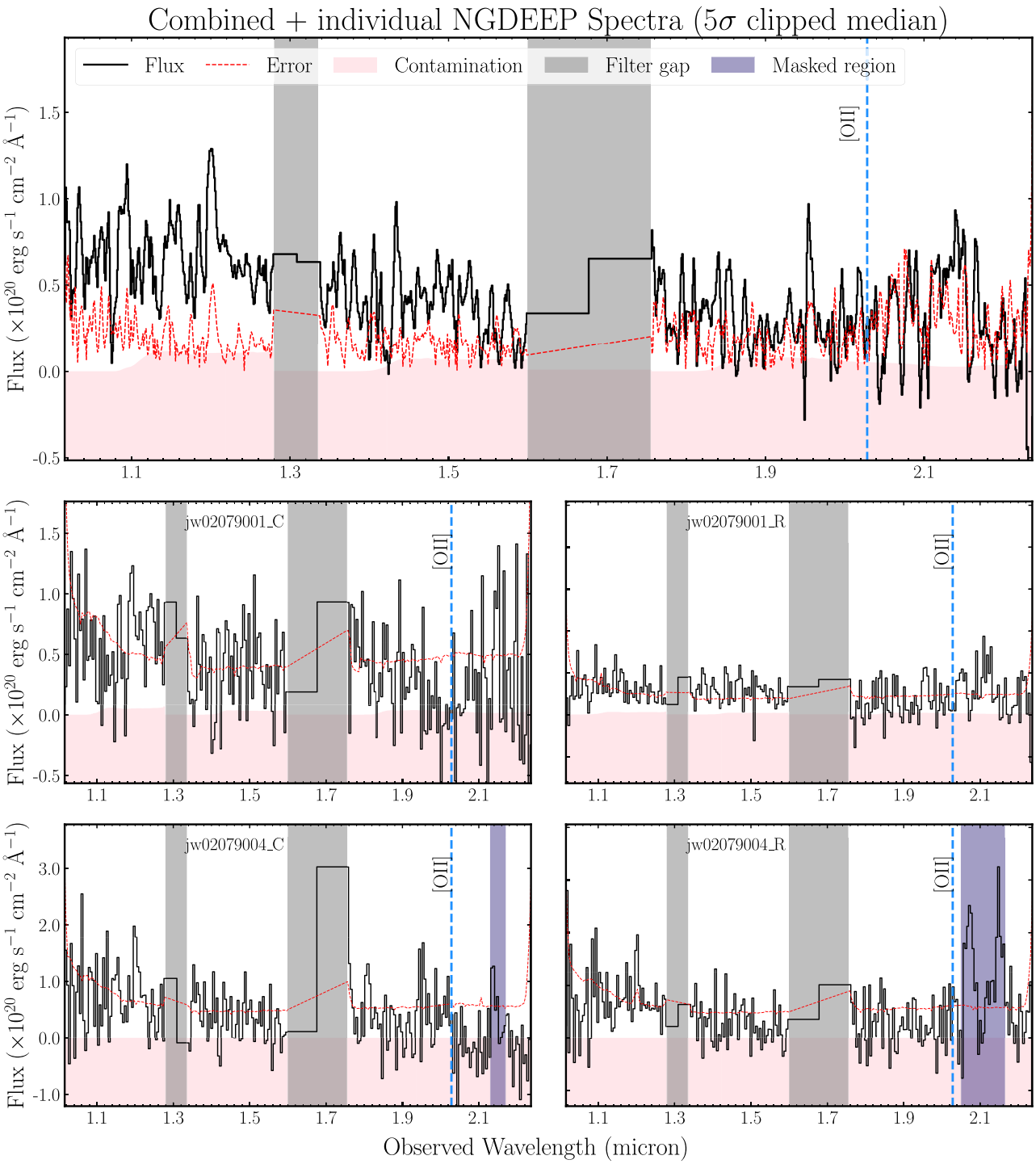

Figure 16. The JWST/NIRISS NGDEEP spectrum of MXDFz4.4 (F115W, F150W and F200W filters). The four individual orientations are shown in the lower panels and the combined (5σ-clipped median) spectrum is shown above. Filter gaps are shaded in gray and contaminants based on the 2D spectra are masked in blue. No lines are detected. The position of [O II] in F200W is shown with a dashed blue line.

ORCID iDs

Ilias Goovaerts https://orcid.org/0009-0007-8470-5946
Marc Rafelski https://orcid.org/0000-0002-9946-4731
Alexander Beckett https://orcid.org/0000-0001-7396-3578
Grecco Oyarzún https://orcid.org/0000-0003-0028-4130
Annalisa Citro https://orcid.org/0009-0000-9676-0538
Farhanul Hasan https://orcid.org/0000-0002-0072-0281
Kalina V. Nedkova https://orcid.org/0000-0001-5294-8002
Calum Hawcroft https://orcid.org/0000-0003-0145-8964
Anton M. Koekemoer https://orcid.org/0000-0002-6610-2048
Mitchell Revalski https://orcid.org/0000-0002-4917-7873
Matthew J. Hayes https://orcid.org/0000-0001-8587-218X
Claudia Scarlata https://orcid.org/0000-0002-9136-8876
Ray A. Lucas https://orcid.org/0000-0003-1581-7825
Norman A. Grogin https://orcid.org/0000-0001-9440-8872
David V. Stark https://orcid.org/0000-0002-3746-2853
Paolo Suin https://orcid.org/0000-0001-7044-3809
Nor Pirzkal https://orcid.org/0000-0003-3382-5941
Louis-Gregory Strolger https://orcid.org/0000-0002-7756-4440

References

Asada, Y., Willott, C., Muzzin, A., et al. 2026, ApJ, 996, 115
Austin, D., Conselice, C. J., Adams, N. J., et al. 2025, ApJ, 995, 43
Bacon, R., Brinchmann, J., Conseil, S., et al. 2023, A&A, 670, A4
Bagley, M. B., Pirzkal, N., Finkelstein, S. L., et al. 2024, ApJL, 965, L6
Bassett, R., Ryan-Weber, E. V., Cooke, J., et al. 2021, MNRAS, 502, 108
Becker, G. D., Bolton, J. S., & Lidz, A. 2015, PASA, 32, e045
Beckett, A., Rafelski, M., Scarlata, C., et al. 2025, ApJ, 992, 155
Beckwith, S. V. W., Stiavelli, M., Koekemoer, A. M., et al. 2006, AJ, 132, 1729
Begley, R., Cullen, F., McLure, R., et al. 2024, MNRAS, 527, 4040
Bielby, R. M., Fumagalli, M., Fossati, M., et al. 2020, MNRAS, 493, 5336
Boquien, M., Burgarella, D., Roehlly, Y., et al. 2019, A&A, 622, A103
Bradley, L., Sipöcz, B., Robitaille, T., et al. 2025, astropy/photutils: v2.3.0, Zenodo, doi:10.5281/zenodo.17129028
Brammer, G. B., van Dokkum, P. G., Franx, M., et al. 2012, ApJS, 200, 13
Brammer, G. B., Whitaker, K. E., van Dokkum,, P. G., et al. 2011, ApJ, 739, 24
Bruzual, G., & Charlot, S. 2003, MNRAS, 344, 1000
Burgarella, D., Buat, V., & Iglesias-Páramo, J. 2005, MNRAS, 360, 1413
Calzetti, D., Armus, L., Bohlin, R. C., et al. 2000, ApJ, 533, 682
Carr, C. A., Cen, R., Scarlata, C., et al. 2025, ApJ, 982, 137
Chabrier, G. 2003, PASP, 115, 763
Chang, H.-C., & Wang, L.-C. 2010, arXiv:1009.4322
Chisholm, J., Saldana-Lopez, A., Flury, S., et al. 2022, MNRAS, 517, 5104
Choustikov, N., Katz, H., Saxena, A., et al. 2024, MNRAS, 529, 3751
Citro, A., Scarlata, C. M., Mantha, K. B., et al. 2025, ApJ, 986, 184
Donnan, C. T., McLure, R. J., Dunlop, J. S., et al. 2024, MNRAS, 533, 3222
Eisenstein, D. J., Willott, C., Alberts, S., et al. 2026, ApJS, 283, 6
Ejdetjärn, T., Östlin, G., Rosdahl, J., Blaizot, J., & Agertz, O. 2026, MNRAS, 546, stag211
Eldridge, J. J., Izzard, R. G., & Tout, C. A. 2008, MNRAS, 384, 1109
Eldridge, J. J., Stanway, E. R., Xiao, L., et al. 2017, PASA, 34, e058
Endsley, R., Stark, D. P., Whitler, L., et al. 2023, MNRAS, 524, 2312
Endsley, R., Stark, D. P., Whitler, L., et al. 2024, MNRAS, 533, 1111
Fan, X., Strauss, M. A., Becker, R. H., et al. 2006, AJ, 132, 117
Finkelstein, S. L., D'Aloisio, A., Paardekooper, J.-P., et al. 2019, ApJ, 879, 36
Finkelstein, S. L., Leung, G. C. K., Bagley, M. B., et al. 2024, ApJL, 969, L2
Flury, S. R., Jaskot, A. E., Ferguson, H. C., et al. 2022a, ApJS, 260, 1
Flury, S. R., Jaskot, A. E., Ferguson, H. C., et al. 2022b, ApJ, 930, 126
Flury, S. R., Jaskot, A. E., Saldana-Lopez, A., et al. 2025, ApJ, 985, 128
Foreman-Mackey, D., Farr, W., Sinha, M., et al. 2019, JOSS, 4, 1864
Foreman-Mackey, D., Hogg, D. W., Lang, D., & Goodman, J. 2013, PASP, 125, 306
Gazagnes, S., Chisholm, J., Schaerer, D., Verhamme, A., & Izotov, Y. 2020, A&A, 639, A85
Giavalisco, M., Ferguson, H. C., Koekemoer, A. M., et al. 2004, ApJL, 600, L93
Gnedin, N. Y., Kravtsov, A. V., & Chen, H.-W. 2008, ApJ, 672, 765
Goovaerts, I., Pello, R., Thai, T. T., et al. 2023, A&A, 678, A174
Goovaerts, I., Thai, T. T., Pello, R., et al. 2024, A&A, 690, A302
Grogin, N. A., Kocevski, D. D., Faber, S. M., et al. 2011, ApJS, 197, 35
Harikane, Y., Nakajima, K., Ouchi, M., et al. 2024, ApJ, 960, 56
Häußler, B., Bamford, S. P., Vika, M., et al. 2013, MNRAS, 430, 330
Hawcroft, C., Leitherer, C., Aranguré, O., et al. 2025, ApJS, 280, 5
Hayes, M., Östlin, G., Atek, H., et al. 2007, MNRAS, 382, 1465
Hayes, M. J., Saldana-Lopez, A., Citro, A., et al. 2025, ApJ, 982, 14
Henry, A., Scarlata, C., Martin, C. L., & Erb, D. 2015, ApJ, 809, 19
Horne, K. 1986, PASP, 98, 609
Hui, L., Stebbins, A., & Burles, S. 1999, ApJL, 511, L5
Inoue, A. K. 2011, MNRAS, 415, 2920
Inoue, A. K., Shimizu, I., Iwata, I., & Tanaka, M. 2014, MNRAS, 442, 1805
Izotov, Y. I., Chisholm, J., Worseck, G., et al. 2022, MNRAS, 515, 2864
Izotov, Y. I., Schaerer, D., Guseva, N. G., Thuan, T. X., & Worseck, G. 2024a, MNRAS, 528, L10
Izotov, Y. I., Schaerer, D., Thuan, T. X., et al. 2016, MNRAS, 461, 3683
Izotov, Y. I., Schaerer, D., Worseck, G., et al. 2018a, MNRAS, 474, 4514
Izotov, Y. I., Schaerer, D., Worseck, G., et al. 2020, MNRAS, 491, 468
Izotov, Y. I., Thuan, T. X., Guseva, N. G., et al. MNRAS, 527, 281
Izotov, Y. I., Worseck, G., Schaerer, D., et al. 2018b, MNRAS, 478, 4851
Jaskot, A. E. 2025, ARA&A, 63, 45
Jaskot, A. E., Silveyra, A. C., Plantinga, A., et al. 2024, ApJ, 972, 92
Ji, Z., Alberts, S., Zhu, Y., et al. 2025, ApJL, 988, L69
Kakiichi, K., & Gronke, M. 2021, ApJ, 908, 30
Kakiichi, K., Ellis, R. S., Laporte, N., et al. 2018, MNRAS, 479, 43
Kennicutt, R. C., Jr. 1998, ARA&A, 36, 189
Kerutt, J., Oesch, P. A., Wisotzki, L., et al. 2024, A&A, 684, A42
Kimm, T., & Cen, R. 2014, ApJ, 788, 121
Koekemoer, A. M., Faber, S. M., Ferguson, H. C., et al. 2011, ApJS, 197, 36
Komarova, L., Oey, M. S., Marques-Chaves, R., et al. 2025, ApJ, 994, 192
Kron, R. G. 1980, ApJS, 43, 305
Le Reste, A., Scarlata, C., Hayes, M. J., et al. 2025, ApJS, 280, 27
Llerena, M., Pentericci, L., Napolitano, L., et al. 2025, A&A, 698, A302
Lofthouse, E. K., Fumagalli, M., Fossati, M., et al. 2020, MNRAS, 491, 2057
Madau, P., Ferguson, H. C., Dickinson, M. E., et al. 1996, MNRAS, 283, 1388
Maji, M., Verhamme, A., Rosdahl, J., et al. 2022, A&A, 663, A66
Markov, V., Bradaç, M., Estrada-Carpenter, V., et al. 2026, A&A, 708, A236
Mary, D., Bacon, R., Conseil, S., Piqueras, L., & Schutz, A. 2020, A&A, 635, A194
Mas-Hesse, J. M., Kunth, D., Tenorio-Tagle, G., et al. 2003, ApJ, 598, 858
Matthee, J., Golling, C., Mackenzie, R., et al. 2024, MNRAS, 529, 2794
Menon, S. H., Burkhart, B., Somerville, R. S., Thompson, T. A., & Sternberg, A. 2025, ApJ, 987, 12
Meštrić, U., Vanzella, E., Beckett, A., et al. 2025, A&A, 698, A203
Muñoz, J. B., Chisholm, J., Sun, G., et al. 2026, MNRAS, 547, stag415
Naidu, R. P., Tacchella, S., Mason, C. A., et al. 2020, ApJ, 892, 109
Nedkova, K. V., Rafelski, M., Teplitz, H. I., et al. 2024, ApJ, 970, 188
Oesch, P. A., Montes, M., Reddy, N., et al. 2018, ApJS, 237, 12
Oke, J. B., & Gunn, J. E. 1983, ApJ, 266, 713
Osterbrock, D. E. 1974, Astrophysics of Gaseous Nebulae Ads (Freeman)
Pahl, A., Topping, M. W., Shapley, A., et al. 2025, ApJ, 981, 134
Pahl, A. J., Shapley, A., Steidel, C. C., Chen, Y., & Reddy, N. A. 2021, MNRAS, 505, 2447
Peng, C. Y., Ho, L. C., Impey, C. D., & Rix, H.-W. 2002, AJ, 124, 266
Peng, C. Y., Ho, L. C., Impey, C. D., & Rix, H.-W. 2010, AJ, 139, 2097
Prichard, L. J., Rafelski, M., Cooke, J., et al. 2022, ApJ, 924, 14
Puschnig, J., Hayes, M., Östlin, G., et al. 2017, MNRAS, 469, 3252
Rafelski, M., Teplitz, H. I., Gardner, J. P., et al. 2015, AJ, 150, 31
Rahner, D., Pellegrini, E. W., Glover, S. C. O., & Klessen, R. S. 2017, MNRAS, 470, 4453
Rieke, M. J., Robertson, B., Tacchella, S., et al. 2023, ApJS, 269, 16
Rieke, M., Robertson, B., Tacchella, S., et al. 2023, Data from the JWST Advanced Deep Extragalactic Survey (JADES), STScI/MAST, doi:10.17909/8TDJ-8N28
Rivera-Thorsen, T. E., Hayes, M., & Melinder, J. 2022, A&A, 666, A145
Rodriguez-Gomez, V., Genel, S., Vogelsberger, M., et al. 2015, MNRAS, 449, 49
Rosdahl, J., Blaizot, J., Katz, H., et al. 2022, MNRAS, 515, 2386
Rudie, G. C., Steidel, C. C., Shapley, A. E., & Pettini, M. 2013, ApJ, 769, 146
Rutkowski, M. J., Scarlata, C., Henry, A., et al. 2017, ApJL, 841, L27
Saldana-Lopez, A., Hayes, M. J., Le Reste, A., et al. 2026, ApJ, 999, 71

Saxena, A., Cryer, E., Ellis, R. S., et al. 2022, MNRAS, 517, 1098
Scarlata, C. M., Hu, W., Hayes, M. J., et al. 2025, ApJ, 985, 115
Schaerer, D., Izotov, Y. I., Worseck, G., et al. 2022, A&A, 658, L11
Shen, X., Vogelsberger, M., Boylan-Kolchin, M., Tacchella, S., & Kannan, R. 2023, MNRAS, 525, 3254
Shibuya, T., Ouchi, M., Harikane, Y., & Nakajima, K. 2019, ApJ, 871, 164
Siana, B., Teplitz, H. I., Colbert, J., et al. 2007, ApJ, 668, 62
Simmonds, C., Tacchella, S., Hainline, K., et al. 2024, MNRAS, 527, 6139
Simmonds, C., Tacchella, S., Maseda, M., et al. 2023, MNRAS, 523, 5468
Sobral, D., & Matthee, J. 2019, A&A, 623, A157
Steidel, C. C., Bogosavljević, M., Shapley, A. E., et al. 2018, ApJ, 869, 123
Steidel, C. C., Pettini, M., & Adelberger, K. L. 2001, ApJ, 546, 665
Sun, G., Faucher-Giguère, C.-A., Hayward, C. C., et al. 2023, ApJL, 955, L35
Sun, L., Wang, X., Teplitz, H. I., et al. 2024, ApJ, 972, 8
Teplitz, H. I., Rafelski, M., Kurczynski, P., et al. 2013, AJ, 146, 159
Trebitsch, M., Blaizot, J., Rosdahl, J., Devriendt, J., & Slyz, A. 2017, MNRAS, 470, 224
Vanzella, E., Nonino, M., Cupani, G., et al. 2018, MNRAS, 476, L15
Verhamme, A., Orlitová, I., Schaerer, D., & Hayes, M. 2015, A&A, 578, A7
Verhamme, A., Orlitová, I., Schaerer, D., et al. 2017, A&A, 597, A13
Wang, X., Teplitz, H. I., Smith, B. M., et al. 2025, ApJ, 980, 74
Williams, C. C., Curtis-Lake, E., Hainline, K. N., et al. 2018, ApJS, 236, 33
Williams, C., Tacchella, S., Maseda, M., et al. 2023, Data from the JWST Extragalactic Medium-band Survey (JEMS), STScI/MAST, doi:10.17909/FSC4-DT61
Williams, C. C., Tacchella, S., Maseda, M. V., et al. 2023, ApJS, 268, 64
Wisotzki, L., Bacon, R., Blaizot, J., et al. 2016, A&A, 587, A98
Yajima, H., Umemura, M., Mori, M., & Nakamoto, T. 2009, MNRAS, 398, 715